HHS Public Access

Author manuscript

Neuron. Author manuscript; available in PMC 2024 July 19.

Published in final edited form as:

Neuron. 2023 July 19; 111(14): 2155–2169.e9. doi:10.1016/j.neuron.2023.04.011.

Age-dependent immune and lymphatic responses after spinal cord injury

Andrea Francesca M. Salvador[1,2,3], **Taitea Dykstra**[1,2], **Justin Rustenhoven**[1,2,4], **Wenqing Gao**[1,2], **Susan M. Blackburn**[1,2], **Kesshni Bhasiin**[1,2], **Michael Q. Dong**[5], **Rafaela Mano Guimarães**[1,2,6], **Sriharsha Gonuguntla**[1,2], **Igor Smirnov**[1,2], **Jonathan Kipnis**[1,2,7,*], **Jasmin Herz**[1,2,*]

[1]Brain Immunology and Glia (BIG) Center, Washington University in St. Louis, St. Louis, MO 63110, USA

[2]Department of Pathology and Immunology, Division of Immunobiology, Washington University in St. Louis, St. Louis, MO 63110, USA

[3]Neuroscience Graduate Program, University of Virginia, Charlottesville, VA 22903, USA

[4]Department of Pharmacology and Clinical Pharmacology, The University of Auckland, Auckland 1023, New Zealand

[5]Thomas Jefferson University Hospital, Philadelphia, PA 19107, USA

[6]Center for Research in Inflammatory Diseases (CRID), Department of Pharmacology, Ribeirão Preto Medical School, University of São Paulo, Ribeirão Preto, São Paulo 14049-900, Brazil

[7]Lead contact

SUMMARY

Spinal cord injury (SCI) causes lifelong debilitating conditions. Previous works demonstrated the essential role of the immune system in recovery after SCI. Here, we explored the temporal changes of the response after SCI in young and aged mice in order to characterize multiple immune populations within the mammalian spinal cord. We revealed substantial infiltration of myeloid cells to the spinal cord in young animals, accompanied by changes in the activation state of microglia. In contrast, both processes were blunted in aged mice. Interestingly, we discovered the formation of meningeal lymphatic structures above the lesion site, and their role has not been examined after contusive injury. Our transcriptomic data predicted lymphangiogenic signaling between myeloid cells in the spinal cord and lymphatic endothelial cells (LECs) in the meninges

*Correspondence: kipnis@wustl.edu (J.K.), herz@wustl.edu (J.H.).

AUTHOR CONTRIBUTIONS

Conceptualization, A.F.M.S., J.H., and J.K.; methodology, A.F.M.S., T.D., J.R., W.G., M.Q.D., I.S., and J.H.; investigation, A.F.M.S., T.D., J.R., W.G., S.M.B., K.B., R.M.G., S.G., M.Q.D., I.S., and J.H.; analysis, A.F.M.S., T.D., M.Q.D., S.G., J.H., and J.K.; visualization, A.F.M.S., T.D., and J.H.; writing, A.F.M.S., J.K., and J.H.; funding acquisition, J.K.; supervision, J.K. and J.H.

SUPPLEMENTAL INFORMATION

Supplemental information can be found online at https://doi.org/10.1016/j.neuron.2023.04.011.

DECLARATION OF INTERESTS

The authors declare no competing interests.

after SCI. Together, our findings delineate how aging affects the immune response following SCI and highlight the participation of the spinal cord meninges in supporting vascular repair.

Graphical Abstract

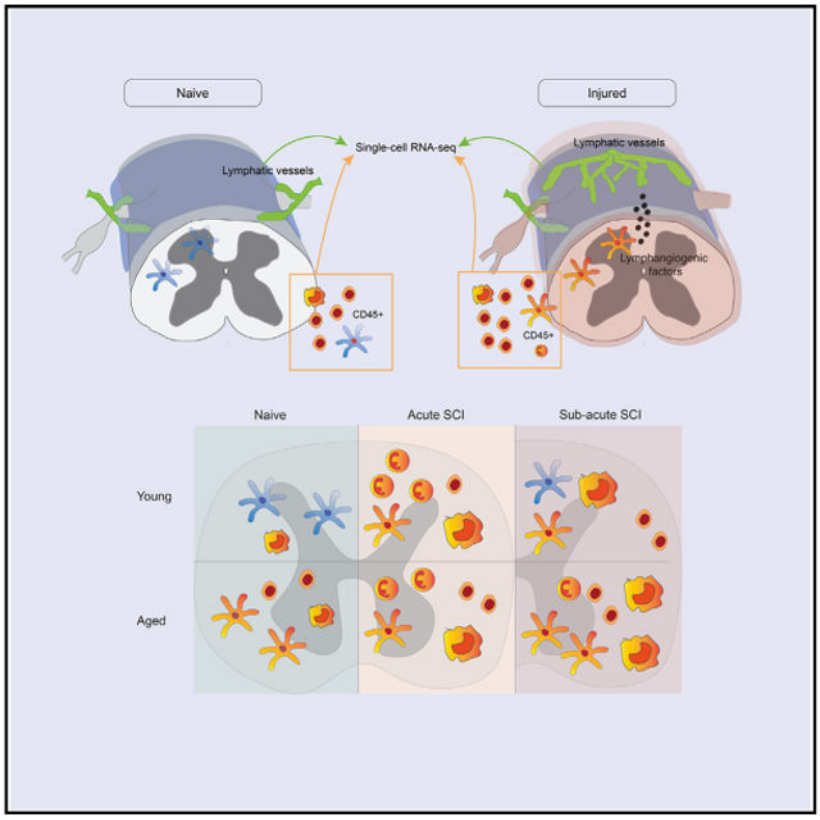

In brief

Salvador et al. identify cellular and transcriptional age-dependent changes in infiltrating and resident immune cells of the spinal cord after contusive injury. They also reveal the formation of ectopic lymphangiogenesis in the spinal cord meninges upon injury, a process directed by myeloid cells.

INTRODUCTION

Traumatic brain injury (TBI) and spinal cord injury (SCI) lead to severe physical, emotional, and economic consequences that dampen patients' quality of life.[1] Patients with SCI have poor prognosis and suffer from lifelong disability due to the limitations of the central nervous system (CNS) to regenerate. The immune response has been reported to hinder recovery after SCI as they can contribute to secondary injury, persistent inflammation, and glial scar formation.[2-8] However, a growing number of studies have since demonstrated that the optimal dynamics of inflammation is integral to wound healing.[9,10] In the CNS, monocyte-derived macrophages and adaptive immune cells–particularly autoreactive T cells–have been shown to be critical for repair[11-16] as they produce growth factors,

phagocytose debris,[17,18] modify the tissue environment, participate in tissue remodeling, and aid in neuroprotection.[19-22] A detailed characterization of the heterogeneity of the immune cells across multiple stages after injury is pivotal in dissecting the immense complexity of the immune response and designing therapies that preferentially augment their reparative properties while mitigating its destructive consequences.

Advancements in single-cell RNA sequencing (scRNA-seq) technologies have led to unbiased profiling of the immune cell heterogeneity in the spinal cord parenchyma following SCI.[23-27] These studies have described the temporal changes in diverse myeloid cell populations and predicted interactions between immune and resident CNS cells that may support the wound healing process. They highlight the importance of microglia in repair,[27-29] but they do not explore the response in the CNS borders–particularly the spinal cord meninges that are also impacted in SCI. The meninges are composed of membranous layers that envelope the CNS parenchyma and is filled with cerebrospinal fluid (CSF) that provides protection to the CNS.[30,31] It harbors functional lymphatic endothelial cells (LECs)[32,33] and a diverse array of innate and adaptive immune cells.[34,35] Cranial meningeal lymphatic vessels can drain CSF, antigens, and immune cells to the cervical lymph nodes, thereby, making this structure critical for shaping the immune responses to the brain.[36-39]

Here, we utilized scRNA-seq to create a comprehensive dataset that profiles the immune cells in the injured spinal cord from young and aged mice where we uncovered major alterations in their composition and transcriptomic signatures during aging. We also assessed the injury response in the spinal cord meninges and found morphological changes in spinal cord meningeal LECs. We hence generated the first scRNA-seq analysis of spinal cord meningeal LECs and determined their changes in aging and after SCI. Using both datasets, we uncovered the expression of angiogenic and lymphangiogenic factors in myeloid cells of the injured spinal cord. Multiple factors were predicted to bind to lymphangiogenic receptors on spinal cord meningeal LECs, suggesting potential functional interactions between the two CNS compartments following SCI. This resource provides molecular insights into the changes during immune aging and furthers our understanding of how the spinal cord meninges may participate in repair.

RESULTS

Aging leads to altered myeloid cell recruitment and increased chemokine induction in macrophages after contusion injury of the spinal cord

Previously published results found that young (2–3 months old) female mice recover better than aged (15–18 months old) female mice after mid-thoracic contusion injury.[40,41] Since the immune response deteriorates with aging, we hypothesized that an in-depth profile of immune populations in young and old mice after SCI may provide important insights into processes that govern recovery after CNS injury. To explore the cellular and molecular alterations in the immune response of aged animals to injury, we employed scRNA-seq of 77,646 immunomagnetically enriched $CD45^+$ cells from the lesion site of the spinal cord of young and aged mice at multiple time points (naive, 3, 7, and 14 days post injury [dpi]) (Figures 1A-1D and S1A). Unsupervised clustering revealed 10 major immune populations in the spinal cord (Figure 1B) based on their expression of known cell-type-specific markers

(Figure 1C; Table S1). Of note is that the leptomeninges surrounding the spinal cord could not be dissected as this membrane collapses onto the parenchyma after contusion (Figure S1B). Dura and arachnoid layers were removed by either PBS flushing or peeling the spinal cord tissue out of the bone (Figure S1C). Comparative analysis identified a few changes in the proportions and gene expression levels of immune cells in aging (Figures 1D and S1D; Table S2). While microglia made up the greatest proportion of $CD45^+$ immune cells in the healthy naive spinal cord, we also detected a small fraction of macrophages, neutrophils, dendritic cells (DCs), and B and T cells. In naive aged mice, we immediately noticed a higher number and frequency of T cells (Figures 1D and S1D; Table S2), in line with studies showing elevated T cell retention in the brain and cranial dura of aged mice.[34,42,43] This was accompanied by up-regulation of genes including the chemokines *Cxcl10*, *Cxcl16, Ccl3*, and *Ccl5* in microglia from aged compared with young mice (Table S3), suggesting that microglia may support T cell recruitment or retention in the aged spinal cord.[44,45]

We next focused on the most profound age-associated changes in immune cell after injury (Figure 1D). At 3 dpi, macrophages, DCs, neutrophils, and monocytes in both young and aged mice significantly expanded in proportion, compared with naive mice (Figure S1E; Table S2). At 7 dpi, the fraction of neutrophils was reduced while macrophages and DCs further increased in young mice but not in aged. At 14 dpi, the proportion of macrophages in young mice decreased from 7 dpi, but this reduction was of a lower degree in aging (Figure S1E; Table S2). Notably, the fraction of monocytes and T cells was higher in the aged samples versus young at all injury time points (Figure S1D; Table S2). Using flow cytometry analysis on an independent cohort of young and aged mice, we validated changes in immune cell populations at steady state and after injury (Figures 1E and S2A-S2C). Both harvesting methods (PBS flushing or peeling spinal cords) had similar yield in immune cell numbers (Figure S2D). While age-associated changes in neutrophils were not observed consistently, alterations included a significant increase in T cells (Figures 1E, S2B, and S2C) and a decrease in proportion and total numbers of macrophages, monocytes, and DCs in aged mice (Figures 1E and S2C).

Peripherally derived myeloid cells can critically influence the outcome of recovery.[2,15,21,46] To reveal their heterogeneity, we subclustered non-granulocytic myeloid cells, which yielded four macrophage, one monocyte, and four DCs clusters (Figures 1F and S2E; Table S4). Parenchymal border macrophages (PBMs), defined by *Mrc1* (CD206) expression,[47,48] were the major population in the young naive spinal cord and leptomeninges (Figure 1G). Inflammatory macrophages were the second most abundant cluster and marked by *Apoe* expression[23] (Figure S2E). Biological pathways related to their function were “myelination” and “gliogenesis” (Figure 1H; Table S4). Recruiting macrophages characterized by *Hmox1* expression[23] were linked to “ATP metabolic process” and “regulation of apoptotic signaling pathway” (Figure 1I). Moreover, recruiting macrophages expressed *Ccl2 and Ccl7*, while PBMs expressed *Ccl12* (Figure 1J), which may promote the recruitment of T cells, monocytes, and DCs.

We next examined the age-associated alterations of myeloid cells. Proportions of PBMs decreased in the naive spinal cord and leptomeninges of aged mice, but recruiting, inflammatory, and proliferating macrophages as well as monocytes were increased,

compared with young mice (Figures 1G and S3A; Table S2). At 3 dpi, all three macrophage populations expanded in proportion in young animals, but proliferating macrophages failed to increase in aged mice (Figure S3B; Table S2). The decrease in proliferating macrophages was supported using flow cytometry analysis of young and aged mice (Figure S3C). At 7 dpi, the proportion of recruiting macrophages in young mice contracted, and inflammatory macrophages further increased (Figure S3D; Table S2). However, the shift in populations was not apparent in aged mice at 7 dpi, which may delay the appearance of macrophages supporting repair (Figures 1H and S3D; Table S2). The composition of macrophage subsets in young and aged spinal cords and leptomeninges did not differ 14 dpi, and a decrease of recruiting macrophages was accompanied by an increase in inflammatory macrophages (Figure S3A). Moreover, we found that the transcriptional signature of injured macrophages in the spinal cord and leptomeninges of aged compared with young mice was enriched for 547 upregulated genes (Figure 1K; Table S4). Related gene ontology (GO) terms such as “reactive oxygen species (ROS) metabolic process,” “positive regulation of cytokine production,” and “ATP metabolic process” (Figure 1L) were identified, suggesting that macrophages infiltrating the injured spinal cord and leptomeninges of aged mice may foster a more inflammatory environment. Thus, we uncovered an initial impairment in myeloid cell recruitment to the injury site (Figures 1D and 1E) and a delayed diversification of macrophages over the course of SCI in aging (Figure 1G), which may contribute to reduced functional recovery in aging.[12]

Activated microglia emerge during aging and display a reduced potential to transition to different states after SCI

Next, we explored microglia heterogeneity and identified four states: (1) homeostatic, (2) activated, (3) interferon (IFN)-responsive, and (4) proliferating microglia[25,49-51] (Figures 2A, 2B, and S4A; Table S4). In the young naive spinal cord, most microglia adopted a homeostatic phenotype (*Tmem119*, *P2ry12*, and *Cx3cr1*[52]), in contrast to aged mice where they were less abundant (Figures 2B and S4B; Table S2). Aged mice featured a population of activated microglia with heightened expression of genes such as *Apoe*, *Axl*, *Cst7*, and *Itgax*, similar to the signature for disease-associated microglia (DAM)[53,54] (Figure 2C). In response to injury, microglia from young mice underwent a striking transformation from expressing homeostatic genes to upregulating activation, proliferation (*Mki67*) or IFN-responsive (*Ifitm3, Isg15*, *Irf7*, and *Stat1*) markers (Figures 2B and S4A; Table S4). From days 3 to 14 post-SCI, proliferating microglia contracted, while homeostatic microglia reappeared, and IFN-responsive microglia continued to expand in young mice (Figures 2B and S4C; Table S2). It has been recently reported that microglia do not return to the original phenotype after SCI.[26] The most striking observation was that in aged animals, activated microglia remained the predominant state across all injury time points. While microglia in aged mice partially retained the capacity to proliferate, IFN-responsive and homeostatic microglia were diminished, as compared with young mice (Figures 2B, S4B, and S4C; Table S2).

To determine the molecular factors that reduce the ability to transition to other states, we compared naive microglia from young and aged mice (Figure 2C). We found that several senescence-related genes (such as *C3*, *Ccl2*, *Cstb*, *Hmgb1*, *Il1b*, *Mif*, *Plau*, and *Cxcl16*) were

upregulated[55] (Figure 2C; Table S3), and their biological processes were linked to “positive regulation of cytokine production,” “ATP metabolic process,” and “cell chemotaxis” (Figure S4D). Examination of downregulated differentially expressed genes (DEGs) revealed their association with pathways such as “regulation of hemopoiesis,” “regulation of inflammatory response,” and “regulation of myeloid cell differentiation” (Figure S4D). The combined effect of senescence, metabolic changes, and decreased capacity to regulate inflammation may contribute to the persistently activated state and reduced plasticity of aged microglia.

We then conducted flow cytometry analysis of the phenotypic changes in microglia in response to injury (Figures 2D, 2E, and S4E). No significant difference in the total number of microglia between young and aged mice was observed (Figure S4E). In accordance with our scRNA-seq results (Figure 2B), the conversion from the P2RY12^{+} homeostatic microglia signature to Ki67^{+}-proliferating and CD11c^{+}-activated microglial signature was evident when comparing naive and injured young mice (Figures 2D and 2E). Of note, this phenotypic change in young mice was in stark contrast to the smaller subset of proliferating microglia and predominantly activated microglia in aging (Figures 2B, 2D, and 2E). In addition, we identified CD68^{+} IBA1^{+} activated microglia by confocal microscopy in the naive spinal cord of aged mice and TMEM119^{+} IBA1^{+} homeostatic microglia in the naive spinal cord of young mice (Figure 2F). At 3 dpi, both young and aged animals harbor proliferating (Ki67^{+} IBA1^{+}) and activated (CD68^{+} IBA1^{+}) cells at the injury site (Figure 2G).

The large fraction of proliferating microglia at 3 dpi in young samples (Figures 2B, 2D, and 2E) prompted us to investigate their differentiation trajectory (Figure 2H). Pseudotime analysis revealed that a subset of proliferating microglia transitions to activated microglia, representing an early response to the injury, which eventually shifts into IFN-responsive microglia, forming a late response (Figure 2H). This raises the possibility that the age-associated increase in activated microglia might represent stagnation in normal differentiation processes. Biological processes related to the marker genes of activated microglia are “oxidative phosphorylation,” “regulation of lipid transport,” and “phagocytosis” (Figure 2I). “Response to IFN-beta (IFNβ),” “antigen processing and presentation,” and “positive regulation of T cell-mediated immunity” were related to IFN-responsive microglia (Figure 2J), hinting that they may sustain T cells in the spinal cord after injury. Expression of *Ccl2* was detected in IFN-responsive and proliferating microglia, while *Ccl12* was expressed in all microglial states (Figure S4F), adding to the production of *Ccl2*, *Ccl7*, and *Ccl12* by macrophages (Figure 1J). To test the role of IFN-responsive microglia, we compared the locomotor recovery of IFN alpha and beta receptor subunit 1 knockout (IFNAR1-KO) mice and their wild-type (WT) littermates after SCI[56] and found no significant difference between groups (Figure S4G). In addition, we assessed the expression of IFNβ and IFN-gamma (IFNγ) in myeloid cells, using yellow fluorescent protein (YFP) reporter mice.[57,58] We found that IFNβ-YFP^{+} cells were concentrated in the lesion site (Figure S4H). Using *in situ* hybridization, we also detected the expression of *Sall1*$^{+}$ *Irf7*$^{+}$ in the lesion site, validating the presence of IFN-responsive microglia (Figure S4I). Using flow cytometry, we did not observe a significant change in the frequency of YFP^{+} microglia between naive controls and 3 dpi, but a modest increase in the total number of IFNβ-YFP^{+} and IFNγ-YFP^{+} CD45^{hi} CD11b^{+} cells was determined (Figures S4J and S4K).

To define the differences in the transcriptomic responses of young and aged microglia after SCI, we combined all microglial clusters and compared them at 3, 7, and 14 dpi (Figures 2K and 2L; Table S3). Shared were 1,006 upregulated DEGs, representing GO terms for "positive regulation of cytokine production," "ATP metabolic process," and "regulation of inflammatory response". Thus, in aged mice, the overrepresentation of pro-inflammatory pathways and shifts in metabolism in microglia were similar to macrophage populations after injury (Figures 1K and 1L).

Contusion injury induces expression of angiogenic and lymphangiogenic factors in myeloid cells of the spinal cord

We next focused on the most profound age-dependent differences between microglia and macrophages of young and aged mice across all injury time points, as compared against naive mice (Figure 3A; Table S5). We identified 191 upregulated and 28 downregulated DEGs shared between young and aged mice that may represent an age-independent transcription program fostered by microglia and macrophages after injury. Among the shared genes are *Ctsb*, *Ctsd*, *Ctsl*, *Ctsz*, *Mif*, and *Cd68* (Table S5), indicating that lysosomal degradation pathways are engaged after injury to clear tissue debris.[59] In young mice, microglia and macrophages upregulated 139 genes, including *Mfge8*, *Timp2*, and *Vegfb* (Table S5) that corresponded to GO terms such as "positive regulation of angiogenesis" and "response to wounding" (Table S5). *Mfge8* and *Timp2* may regulate the severity of tissue fibrosis and remodeling in lung and cardiac injury, respectively.[60,61] The total fraction of downregulated DEGs was much higher (362) and included *Il6ra* and *Ptgs1* (Table S5), indicating that microglia and macrophages in young mice have an increased capacity to remodel tissue and promote faster resolution of inflammation.

Myeloid cells can facilitate the repair of vascular damage after cerebrovascular injury and TBI.[62] To further determine if myeloid cells support this function after SCI, we surveyed the expression of angiogenic and lymphangiogenic factors (Figure 3B) and found *Pdgfb*, *Pdgfa*, *Igf1*, and *Vegfb* primarily expressed in diverse states of microglia and macrophages. However, *Hpse*, *Hgf*, and *Vegfa* were mostly expressed in various macrophage populations. *Pdgfb* and *Tnf*, on the other hand, showed increased expression levels in microglia compared with macrophages. Overall, aged mice exhibited higher expression levels of angiogenic and lymphangiogenic factors across multiple myeloid cell types (Figure 3B). Therefore, we further analyzed and validated protein expression of vascular endothelial growth factor (VEGF) in naive and injured spinal cords, using a pan-VEGF antibody (Figures 3C-3E). In spinal cords of injured mice, we confirmed that $VEGF^+$ $IBA1^+$ myeloid cells were detectable at the injury site (Figure 3D). VEGF coverage, however, was not significantly different between injured spinal cords of young and aged mice on day 3 post-SCI (Figure 3E).

Recent studies demonstrated that the vertebral column harbors *bona fide* lymphatic vessels in the meninges that facilitate the drainage of solutes to peripheral lymph nodes and respond to VEGF-C and demyelinating SCI.[63] We therefore examined VEGF expression on whole-mount preparations of the spinal cord meninges (Figures 3F and 3G). Interestingly, the localization of VEGF in the naive meninges was uniformly distributed but became more

concentrated near the lesion site at 3 and 7 dpi (Figure 3F). At 11 dpi, a ring of VEGF was detected surrounding $CD31^+$ blood vessels, suggesting VEGF-mediated angiogenesis in the meninges (Figure 3G). While we detected *Vegfa* and *Vegfb* transcripts in the spinal cord and leptomeninges, *Vegfc* was minimally expressed (Figure 3B). However, *Vegfc* mRNA expression was highly induced in the spinal cord dural meninges shortly after contusion injury (Figure 3H). Collectively, these results demonstrate that resident and infiltrating myeloid cells undergo both, age-dependent and -independent transcriptional programs in response to contusion. One of the shared processes that occurs in the spinal cord is the regulation of angiogenesis.

Macrophages mediate remodeling of spinal cord meningeal lymphatic vessels after injury

Because VEGF-C induces lymphangiogenesis,[64,65] we examined the focal spinal cord lesion site for the presence of lymphatic vessels in the dural meninges (Figures 4A and 4B). Within 6 days after injury, we observed the formation of $LYVE1^+$ $VEGFR3^+$ lymphatic vessels in a few mice at the contusion site. Measuring their surface area over time revealed that lymphangiogenesis significantly increased on day 10 and peaked at day 16 post-SCI (Figure 4B). This contrasts with naive conditions where the spinal cord meningeal lymphatic vessels only surround nerve roots[37,63,66] and $LYVE1^+$ cells predominantly representing $VEGFR3^-$ macrophages. Notably, the ectopic formations, which we refer to as the “lymphatic patch” hereafter, were also caused by laminectomy (Figure S5A), which is performed to expose the spinal cord for contusion injury and subdural injections (Figures 4C-4G and S5B). Thus, lymphangiogenesis was specifically induced at sites of injury.

Given the expression of angiogenic and lymphangiogenic factors in myeloid cells in the spinal cord after injury (Figures 3B-3E), we hypothesized that resident macrophages may be partially involved in the expansion of spinal cord lymphatics in the meninges. To test this hypothesis, we depleted macrophages in the spinal cord meninges using laminectomy and subdural injections of liposomes containing clodronate (Figures 4E-4G). Within 1 week, more than 70% of $CD206^+$ meningeal macrophages were depleted (Figure 4F), and concurrently, the coverage of the $LYVE1^+$ lymphatic patch induced by the laminectomy significantly reduced in size (Figure 4G). These results suggest that local macrophages drive lymphangiogenesis near the injury site. It is possible, however, that this process may also be supported by perivascular macrophages and infiltrating myeloid cells such as $Ly6C^+$ monocytes (Figure S5C).

scRNA-seq reveals a potential lymphangiogenic signaling axis between spinal cord myeloid and meningeal LECs after injury

We postulated that spinal cord meningeal lymphatics are contributing to the poor recovery of aged mice after SCI. To test this, we employed deep (1 million reads per cell) single-cell sequencing of FACS-enriched LECs (viable $CD45^-$ $PDPN^+$ $LYVE1^+$ $CD31^+$) from the spinal cord meninges of naive and 3 dpi young and aged mice (Figures 5A-5G; Table S6). Visualization of ~360 LEC transcriptomes using t-distributed stochastic neighbor embedding (tSNE) revealed their segregation based on age and injury status (Figure 5B). In LECs from young mice, analysis of upregulated genes and their associated GO terms demonstrated a strong response to wounding and regulation of angiogenesis after SCI (Figures S5D and

S5E). Importantly, in aged LECs, injury to the spinal cord involved similar DEGs and GO biological processes (Figures S5F and S5G). However, directly comparing LECs from young and aged mice revealed various downregulated DEGs after injury (Figures 5D and 5E) such as *Adamts4*, *Cldn11*, *Col5a1*, *Col6a2*, and *Mmp2* (Figure 5E), associated with the organization of the extracellular matrix and vasculature (Figure 5F). In addition, LECs from aged mice featured increased expression of genes for cytokines (*Cx3cl1*), chemokine (*Ccl6*), MHCII (*H2-Ab1*), neuropeptide (*Tac1*), and complement (*C1qa* and *C1qb*) 3 days post-SCI (Figure 5E; Table S6). Some of the upregulated DEGs in aged versus young LECs corresponded to the GO pathways “response to temperature stimulus,” “vesicle-mediated transport in synapse,” and “sensory perception of pain” (Figure 5F), suggesting potential LEC interactions with the peripheral nervous system that may underlie increased pain persistence after injury in aging.[67,68]

Our immune cell profiling revealed increased expression of several lymphangiogenic factors in microglia and macrophages of the injured spinal cord (Figure 3B). To determine if LECs from young and aged mice differ in lymphangiogenic growth factor signaling, we examined the expression of receptors and co-receptors (Figure 5G). Notably, 3 days post-SCI, we observed up-regulation of *Kdr* (VEGFR2) and *Flt4* (VEGFR3) in aged LECs. However, in young mice, *Flt4* expression together with *Fgfr1* was significantly decreased, compared with naive controls. While *Ptger4* was only detected in aged LECs, we saw expression of *Pdgfrb* only in young LECs. VEGFR co-receptors, *Nrp1* and *Nrp2*, were expressed in all groups, and *Nrp2* expression increased after injury independent of age. Expression of anti-lymphangiogenic factors including *Cd36*, *Il4ra*, and *Il17ra*[69] were also detected in spinal cord meningeal LECs.

To further delineate potential interactions between myeloid cells and meningeal LECs in the spinal cord after injury, we paired lymphangiogenic growth factors derived from macrophages and microglia of injured young and aged spinal cords 3 dpi (Figure 3B), with lymphangiogenic receptors expressed in meningeal LECs 3 dpi (Figure 5G). Notably, interaction of *Vegfa* and *Vegfb* with *Kdr* was observed in young and aged samples, but *Vegfc* was only present in young cells despite detectable receptor expression in both groups (Figure 5H). Looking more closely at the lymphangiogenic factors in LECs from aged mice, *Igf2* was uniquely identified (Figure 5H) and possibly supplied by PBMs (Figure 3B). Most other interactions were present in both young and aged but differed in magnitude (e.g., *Igf1-Igfr*), indicating that aged LECs may require enhanced signaling as reported in cutaneous wounds.[70] Together, these findings suggest that myeloid cells of the spinal cord promote injury-associated lymphangiogenesis in the meninges, representing a previously undescribed function that can be targeted to improve recovery.

DISCUSSION

Tissue injury triggers the immune system to facilitate repair, and its optimal resolution is necessary to prevent damage. Here, we describe the cellular and molecular changes in the immune response occurring in the spinal cord and the meningeal lymphatic vessels after SCI, as well as how these are altered in aging. Upon contusion, we uncovered an age-related delay in the recruitment of peripherally derived myeloid cells and impaired ability of

microglia to shift transcriptional states. Moreover, we demonstrated immune cell-mediated lymphangiogenesis of spinal cord meningeal LECs and showed their transcriptional program after injury.

Peripherally derived myeloid cells recruited to the injured spinal cord modulate recovery by engaging in debris clearance, release of growth factors, and remodeling.[18,21,71] Infiltration of myeloid cells to the injured spinal cord occurred in young mice but was significantly reduced in aging. The recruitment of peripheral myeloid cells not only initiates the clearance process but also signals the termination of inflammation.[72] The adjacent skull and vertebral bone marrow have been recently shown as a reservoir of myeloid cells that promptly supplies the inflamed or injured CNS.[73-76] Because CNS-associated bone marrow may be more beneficial to repair than its blood-derived counterparts,[73] strategies that preferentially mobilize these cells to the spinal cord during injury and aging should be explored. Furthermore, delivery of chemotactic signals derived from the injured tissue may be impaired because of altered CSF movement in aging.[77]

Aside from changes in cell recruitment, the proportion of PBMs recently shown to modulate CSF dynamics in the brain in aged animals is reduced, compared with young animals.[48] The reduction in aging may affect fluid movement in the spinal cord, and further characterization of this population may lead to rejuvenation strategies that can improve outcome. Aside from PBMs and proliferating macrophages, molecular profiling revealed two other subclusters: inflammatory and recruiting macrophages in the spinal cord. The shift in population similarly reported in young spinal cords[23] is absent in aged samples. Signals in the local environment may continuously support this population, or cell intrinsic or epigenetic marks prevent their timely differentiation. Fate-mapping studies using markers derived from our molecular analysis can be utilized to determine the function of these macrophages. Prior studies have indicated that elevated levels of ROS in macrophages from middle-aged mice can impede functional recovery after SCI.[4,78] Examining alterations in macrophage metabolism that enhance ROS signaling during the aging process could reveal potential targets for modulation, ultimately leading to improved repair mechanisms.

Profiling of microglia in young mice revealed that from a homeostatic, uninjured state, they adopt a signature reminiscent of the DAM profile identified in models of neurodegeneration after contusion.[53,54] The activated microglia we observed downregulated homeostatic genes and upregulated several genes related to DAMs.[79] A similar signature has been described in spinal cord contusion injury,[23,26,27,80] suggesting that the induction of the DAM or activated microglia phenotype may be conserved in response to damage in the CNS. Functionally, the inability to induce DAMs leads to worsened compaction of amyloid plaques and neuronal damage,[81,82] indicating that they are critical for restricting neurodegeneration. Likewise, activated microglia expressed genes associated with lipid localization, chemotaxis, and phagocytosis–processes that are necessary for attenuating the damage and release of myelin debris after contusion. Impairing microglial activation through the selective depletion of genes critical for this transition, e.g., *Trem2* and *Syk*,[83,84] may be employed to define its role in the context of SCI.

Unlike young animals, aged mice harbor microglia with an activated signature even in the absence of injury. Interestingly, the aged naive spinal cord also contains increased T cell numbers, which we predict to be supported by the enhanced chemokine expression of activated microglia. Increased expression of adhesion factors and type I IFN signaling[85] in the aged spinal cord may further enhance the retention and survival of T cells. It is possible that the increased T cell numbers[86] and intracellular changes in aged microglia[87] contribute to their persistent activated signature. Strategies such as depletion of T cells or reprogramming of activated microglia in aged mice present appealing options for maintaining the microglial homeostatic status, which could potentially enhance recovery outcomes.

Revascularization is integral to resolving tissue damage in the CNS.[62,88] Our data revealed that both resident and recruited myeloid cells express angiogenic and lymphangiogenic factors, and we observed induction of VEGF expression in the injury site 3 days after injury. VEGF was also induced in the injury site in the spinal cord meninges, and surprisingly, it was in close apposition to blood vessels, suggesting productive vasculogenic signaling in the bordering tissue. Interestingly, *Vegfc* was minimally detected in the spinal cord, but it was highly induced in the meninges after contusion injury and meningeal macrophage dependent. It would be of interest to dissect the contributions and interactions of parenchymal and meningeal macrophages in the revascularization process, as well as age-related changes in the spinal cord meningeal compartment that can lead to worsened recovery. More recently, the aged cranial meningeal immune response after TBI was described, and like the aged spinal cord, displayed pre-existing activation.[89]

The function of the lymphatic patch in the meninges after SCI has yet to be addressed as it requires the development of focal ablative strategies, but in cardiovascular injuries, augmentation of lymphangiogenesis led to a significant reduction of inflammation and edema that improved recovery.[90] Our data suggest that upon injury, spinal cord meningeal LECs foster cellular programs that are related to tissue remodeling, matrix organization, and repair. Moreover, upregulated DEGs of aged, injured LECs are related to the sensory perception of pain. This unexpected finding may indicate that LECs interacting with the surrounding nerve roots in the spinal cord may modulate pain, especially after injury. Honing in on this interaction can lead to the development of new pain management therapies.

Overall, our results indicate that the immune response after SCI is not limited to the parenchyma as active changes in the spinal cord meningeal immune cells transpire. Our study puts the spotlight on the spinal cord meninges, which remains understudied in CNS injury and in neurodegenerative diseases. Future investigations should focus on the complex and dynamic interactions between the CNS compartments–the parenchyma, meninges, and the surrounding bone marrow–as they may be necessary to promote functional recovery after injury.

Limitations of the study

Comparative analysis between mouse and human SCI patients presents a challenge due to the difficulties to obtain human spinal cord tissue and the lack of publicly available

datasets. Studies comparing the transcriptional profiles of rodents and humans describe notable species differences in the signatures of microglia, astrocytes, and oligodendrocytes in neurodegeneration of the brain.[91] In the future, it should be determined if the cell types and cell states recapitulated in experimental rodent models exist in humans, given the variability of human SCI. One other limitation is the performance of our scRNA-seq dataset with no technical replicate. Instead, cells from 3 to 5 mice were pooled per group as an effective strategy to reduce technical variations. To better capture biological variability, we therefore provided flow cytometry analysis on an independent cohort to determine cellular changes after injury. Lastly, aged mice are usually larger than young mice, and a different impactor tip may be necessary to fully contuse the spinal cord. While both young and aged mice similarly succumb to immediate locomotor deficits after injury, complex differences in body size, body composition, energy expenditure, and behavior (e.g., sleep, activity, and feeding) were not controlled for in our study. Predictions from physiological data might be feasible in the near future.[92]

STAR★METHODS

RESOURCE AVAILABILITY

Lead contact—Further information and requests for resources and reagents should be directed to and will be fulfilled by Jonathan Kipnis (kipnis@wustl.edu).

Materials availability—This study did not generate new reagents or mouse lines.

Data and code availability

- Fastq files and quantified gene counts for single-cell sequencing are available at Gene Expression Omnibus (GEO) and Sequence Read Archive (SRA) under the accession number GEO: GSE205038.
- Custom code used to analyze the RNA sequencing data is freely available at (https://doi.org/10.5281/zenodo.7604317).
- Any additional information required to reanalyze the data reported in this paper is available from the lead contact upon request.

EXPERIMENTAL MODEL AND SUBJECT DETAILS

Animals—Mice were bred in-house, purchased from the Jackson Laboratory, or provided by the National Institutes of Health, National Institutes of Aging. Female mice were used in all experiments. Mice were housed under pathogen-free and temperature- and humidity-controlled conditions with a 12-hour light cycle. Mice were housed with no more than five animals per cage with regular rodent chow and water provided *ad libitum*. Mice purchased were allowed to habituate for at least one week in the animal facility prior to experimentation. The following strains were used in this study: C57BL/6J (WT, JAX 000664), B6(Cg)-*Ifnar1*$^{tm1.2Ees}$/J (IFNAR1-KO, JAX 028288), B6.129-*Ifnb1*^{tm1Lky}/J (IFNβ-YFP, JAX 010818), and C.129S4(B6)-*Ifng*$^{tm3.1Lky}$/J (IFNγ-YFP, JAX 017581). Unless otherwise stated, mice were tested at 2-4 months of age (young) or 18-24 months of age (aged). All experiments were approved by the Institutional Animal Care and Use

Committee at Washington University in St. Louis (20-0043) and/or the University of Virginia.

METHOD DETAILS

Spinal cord contusion injury—Mice were anesthetized with a ketamine (100 mg/kg)-xylazine (10 mg/kg) mixture. The skin over the dorsal thoracic area was shaved and cleaned with alternating betadine and alcohol swabs. A 15-mm midline skin incision was made, and the connective tissue and muscles were bluntly dissected to expose T6-T13. Laminectomy was performed at T9 to expose the dorsal spinal cord, and the vertebral column was stabilized with angled clamps attached to the T7 and T12 transverse processes. The contusion injury was delivered using an Infinite Horizon Impactor (IH-0400 Impactor) using a standard 1.3 mm impact tip with a force of 90 kDynes. After injury, the muscles and skin were sutured separately. Mice were given subcutaneous and intraperitoneal injections of buprenorphine (0.05 mg/kg) and antibiotics (2.5 mg/kg), respectively for post-operative analgesia and prophylaxis against urinary tract infections. The mice were given soft food for up to two weeks, and their bladders were manually expressed 2 times a day for the duration of the experiments.

To measure functional recovery after injury, the mice were scored every other day by an experimenter blinded to the experimental groups using the metrics described in the Basso mouse scale for locomotion (BMS).[56] Of note is that there was no difference in the locomotor recovery between young and aged groups in the first week following injury,[40] indicating that groups had similar locomotor deficits following 70 kDyn contusion SCI.

Tissue collection and immunohistochemistry—Mice were euthanized with an intraperitoneal injection of Euthasol or Fatal-Plus (10% v/v), followed by transcardial perfusion of ~20 ml PBS with 5 U/mL of Heparin and for lymphatic vessel assessment with 10 ml 4% paraformaldehyde (PFA). The dorsal skin of the back was cut, and the vertebral column was removed and post fixed in 4% PFA at 4°C for 16-48 hours. The ventral bone of the vertebrae was cut laterally and was removed to expose the spinal cord. Nervous tissue was carefully dissected from the bone using fine forceps to release the dorsal root ganglia surrounded by the meninges. The meninges was cut along the ventral side and peeled from the spinal cord. Tissues were stored in PBS until further use. Spinal cords were transferred to 30% sucrose for an additional 24-48 hours at 4°C until the tissue has sunk. After cryopreservation with sucrose, spinal cords were embedded in molds with OCT gel and frozen using dry ice. Frozen tissue blocks were kept at −20°C. They were sectioned into 30 μM sagittal slices that were mounted on gelatin-coated slides, and slides were kept at −20°C until further use.

To prepare whole vertebral column sections, a segment of the intact vertebral column was collected, and the adjoining muscles and fat were scraped off to clean the tissue. The sample was decalcified using Morse's solution (20% formic acid, 10% sodium citrate in distilled water) at 37°C overnight with agitation. After incubation, tissue was washed with PBS and transferred to 30% sucrose for an additional 24-48 hours at 4°C until the tissue has sunk. After cryopreservation with sucrose, samples were embedded in molds with OCT gel and

frozen using dry ice. Frozen tissue blocks were sectioned into 30 μM coronal slices that were mounted onto gelatin-coated slides for further use.

Frozen spinal cord and whole vertebral sections on gelatin-coated slides were allowed to thaw in PBS for 5 minutes at RT. After thawing, the slides were dried, and the edges were lined using a hydrophobic barrier pen. The sections were blocked and permeabilized were blocked and permeabilized in blocking buffer (PBS with 1% BSA, 0.1 % Triton X-100, 0.05% Tween 20 and 2% donkey or chicken serum) for 1 hour at RT. The blocking solution was aspirated, and the sections were incubated with primary antibodies in staining buffer (PBS with 1% BSA and 0.5% Triton X-100) at 4°C for 16-24 hours. They were then washed three times with PBS for 10 minutes at RT. The samples were incubated with secondary antibodies in staining buffer at RT for 1 hour. After incubation, samples were washed once with DAPI (1 μg/mL) in PBS for 10 minutes at room temperature and washed twice with PBS. The slides were then dried, and cover slipped with FluorSave reagent (Millipore).

Spinal cord meninges were blocked and permeabilized in blocking buffer (PBS with 1% BSA, 0.1 % Triton X-100, 0.05% Tween 20 and 2% goat or chicken serum) for 1 hour at room temperature (RT) in 24-well plates with agitation. Samples were incubated with an optimal concentration of primary antibodies in staining buffer (PBS with 1% BSA and 0.5% Triton X-100) at 4°C for 16-24 hours with agitation and washed three times with PBS for 10 minutes at RT. If required, the samples were incubated with secondary antibodies in staining buffer at RT for 1 hour with agitation. After incubation, samples were washed once with DAPI (1 μg/mL) in PBS for 10 minutes at room temperature and washed with PBS. The meninges were mounted in Superfrost Plus slides (Fisher Scientific) and cover slipped with FluorSave reagent (Millipore).

RNAscope *in situ* hybridization—Mice were euthanized with an intraperitoneal injection of Euthasol or Fatal-Plus (10% v/v) and perfused with ice-cold ~20 ml PBS with 5 U/mL of Heparin followed by ~15 mL of pre-chilled neutral buffered formalin (NBF) (Fisher Scientific). Vertebral columns were harvested from the perfused animals and were kept in NBF for 24 hours at 4°C. After fixation, the spinal cords were dissected from the bone as described above. Spinal cords were immersed at 4°C in increasing concentrations of sucrose (10%, 20%, 30% in 1X PBS) with each step lasting until the tissue sunk at the bottom of the tube. After incubation with 30% sucrose, the spinal cords were embedded in molds and frozen using OCT gel using dry ice. Sagittal sections of 15 μM thickness were prepared, mounted onto Superfrost plus slides, and treated following instructions for fixed frozen tissue samples (RNAscope® Multiplex Fluorescent Reagent Kit v2 Assay). Briefly, the frozen sections were washed with 1X PBS for 5 mins followed by incubation at 60°C for 30 mins. Afterwards, slides were immersed in pre-chilled 10% NBF for 15 mins at 4°C and dehydrated in an ethanol series (50%, 70%, 100%, 100%). Dehydrated samples were treated with hydrogen peroxide for 10 mins at RT, boiled with 1X Target Retrieval Solution for 5 mins, washed with dH2O, and rinsed with 100% ethanol. The samples were incubated with Protease Plus at 40°C for 30 mins. The hybridization and amplification steps were followed as instructed by the manual. The following probes were utilized: *Irf7* (Mm-Irf7-C1) and *Sall1* (Mm-Sall1-C3). Detection of *Irf7* expression on *Sall1*$^{+}$ microglia was achieved using Opal 690 (1:1000, Perkin Elmer) and Opal 570 (1:1500, Perkin Elmer), respectively. Nuclei

were counterstained with DAPI at RT for 30s. Slides were mounted using ProLong Gold reagent (Thermo Fisher), and cover slipped.

Confocal and widefield microscopy—Slides were stored at 4°C and images were acquired using a fluorescent slide scanner (Olympus VS200) with a 10 or 20x objective with 0.70 NA and confocal microscopy (Stellaris X8 confocal system or Leica TCS SP8, Leica Microsystems) with the LASX AF Soft-ware. Quantitative analysis was performed blinded using the Fiji package for ImageJ. For coverage measurements, a threshold to identify positive signal was assigned manually, and they were quantified as area of signal/total area of the site as determined by DAPI coverage. All imaging and thresholding parameters were identical for all groups to eliminate experimental bias.

Subdural injections—Mice were anesthetized with a mixture of ketamine (100 mg/kg)-xylazine (10 mg/kg). The dorsal skin over the thoracic to lumbar area was shaved and cleaned with alternating betadine and alcohol swabs. An incision was made in the shaved back, and a small opening was made in the muscles around the left and right side of the interspace between T8 and T10. Laminectomy at T9 was performed. A Hamilton syringe fitted with a 33-gauge needle was then inserted through the intervertebral space and under the dura mater, and 2 μL of clodrosomes (clodronate-containing liposomes, Fisher Scientific), encapsomes (control liposomes), or fluoroliposomes (fluorescent liposomes) were injected. After injection, the skin was sutured, and the mice were given subcutaneous injection of ketoprofen (2.5 mg/kg) as post-operative analgesia. The mice were sacrificed 7 days post injection for further analysis.

Single-cell suspension—Mice were euthanized with an intraperitoneal injection of Euthasol or Fatal-Plus (10% v/v), followed by transcardial perfusion of PBS with 5 U/mL of Heparin. Vertebral columns were obtained and trimmed to only include 1 cm surrounding the lesion site. The ventral bone of the vertebrae was cut laterally and was removed to expose the spinal cord. Nervous tissue was carefully dissected from the bone using fine forceps to release the dorsal root ganglia. The spinal cord dural meninges was cut along the ventral side and peeled from the spinal cord. To compare the immune cell composition between peeled and flushed preparations, spinal cords were also flushed from the ventral bone using an 18-gauge PBS-filled syringe.

The spinal cord (consisting of parenchyma and leptomeninges) was mechanically dissociated with scissors and then digested with prewarmed RPMI (Gibco) containing 1 mg/mL collagenase VIII (Sigma Aldrich), 0.5 mg/mL DNase I (Sigma Aldrich), and 2% FBS (Gibco) for 30 minutes at 37°C with trituration every 15 minutes. The enzymes were neutralized using RPMI with 10% FBS. Samples were passed through a 70 μm filter to obtain single-cell suspensions, washed with FACS buffer, and pelleted at 380 g for 5 minutes. The pellet was resuspended in a 3:1 solution of 22% BSA and FACS buffer (1% BSA, 25 mM HEPES, 1 mM EDTA in PBS) and centrifuged at 1000 g for 10 minutes. The myelin-containing upper layer was aspirated. The clarified cell pellet was washed and resuspended in ice-cold FACS buffer and kept on ice until use.

The spinal cord meninges were enzymatically digested with prewarmed RPMI containing 1 mg/mL collagenase VIII, 0.5 mg/mL DNase I, and 2% FBS for 30 minutes at 37°C for 30 minutes with trituration every 15 minutes. The enzymes were neutralized using RPMI with 10% FBS. Samples were passed through a 70 μm filter to obtain single-cell suspensions, washed with FACS buffer, and pelleted 380 g for 5 minutes. Myelin was removed from the meninges using the procedure described above. The cell pellet was resuspended in ice-cold FACS buffer and kept on ice until use.

Flow cytometry—Single-cell suspensions were transferred into V-bottom well plates and pelleted. Samples were incubated with Zombie NIR fixable viability dye (Biolegend) diluted at a 1:500 in PBS for 20 minutes at 4°C. Samples were centrifuged and resuspended in FACS buffer with CD16/32 FC block (Biolegend) at a final concentration of 5 μg/mL. They were incubated at 4°C for 5 minutes. For surface staining, fluorescently conjugated antibodies resuspended in FACS buffer supplemented with Brilliant Stain Buffer Plus (BD Biosciences) were added to the cell suspension, and the resulting cell suspension was incubated at 20 minutes for at 4°C. Samples were washed and resuspended in FACS buffer. They were run on the Cytek Aurora spectral flow cytometer, and the data was analyzed using FlowJo software (BD). For intracellular Ki67 staining, surface staining was performed as described above, and cells were fixed/permeabilized using the Foxp3/Transcription factor staining buffer set (eBioscience). Cells were stained for 30 minutes at 4°C with fluorescently conjugated antibodies targeting intracellular antigens. After intracellular staining, cells were washed and resuspended in FACS buffer. They were run on the Cytek Aurora spectral flow cytometer (5 lasers: UV-V-B-Y-R), and the data was analyzed using FlowJo software (BD).

RNA isolation and quantitative real-time PCR assay—Spinal cord meninges were peeled from the spinal cords of PBS perfused mice as described above. The tissue was dissociated with TRIzol reagent using silica beads (Biospec Products) and homogenization (Mini bead beater, Biospec Products). Total RNA was extracted from the tissue using the RNAqueous Micro Total RNA Isolation Kit (Thermo Fisher) and DNase I treatment performed. RNA was converted using the High-capacity cDNA reverse transcription kit (Applied Biosystems) diluted with 9 uL of SYBR green (iTaq Universal Supermix, Bio-Rad). Gene expression of *Vegfc* was determined by qPCR and was normalized to *Gapdh.*

Single-cell RNA sequencing for immune cells of the spinal cord using the 10X platform

Cell isolation and enrichment: Vertebral columns obtained after perfusion and cut to include 1 cm around both sides of the lesion site. Spinal cords were flushed from the vertebral column using a PBS-filled syringe. Spinal cords (consisting of parenchyma and leptomeninges, Figures S1D and S1F) were enzymatically digested, as described above, and $CD45^+$ cells enriched from the spinal cord single-cell suspensions following the protocol for $CD45^+$ microbeads (Miltenyi Biotec) and LS columns (Miltenyi Biotec). Two spinal cords per sample were pooled and applied to each column. Isolated cells per sample were pooled and were passed through the column again to increase purity. Cells were resuspended to a concentration of 1000 cells/uL in PBS supplemented with 0.04% non-acetylated BSA (Thermo Fisher Scientific).

Single-cell RNA sequencing: The $CD45^+$ cells enriched from the spinal cord were loaded onto a 10X Genomics Chromium platform for GEM and cDNA generation with cell- and transcript-specific barcodes and sequencing libraries made using the Chromium Single Cell 3' Library and Gel Bead Kit v3. Libraries were then sequenced using the Illumina NovaSeq6000 targeting 100,000 reads per cell.

Single-cell data preprocessing: Reads were aligned to the mm10 genome using the Cellranger software pipeline (version 6.0.0) provided by 10x Genomics. The resulting filtered gene by cell matrix of UMI counts was read into R using the read10xCounts function from the Droplet Utils package. Filtering was applied to remove low quality cells. The exclusion criteria filtered out cells expressing fewer than 200 or greater than 7,500 unique genes, cells having fewer than 1,500 or greater than 60,000 UMI counts, and cells with greater than 20% mitochondrial gene expression. Expression values for the remaining cells were then normalized using the scran and scater packages. The resulting $\log_2$ values were transformed to the natural log scale for compatibility with the Seurat (v3) pipeline.[94-96]

Dimensionality reduction and clustering: The filtered and normalized matrix was used as input to the Seurat pipeline, and cells were scaled across each gene before the selection of the top 2,000 most highly variable genes using variance stabilizing transformation. Principal Components Analysis was conducted, and an elbow plot was used to select the first thirteen principal components for tSNE analysis and clustering. Shared Nearest Neighbor (SNN) clustering optimized with the Louvain algorithm, as implemented by the Seurat *FindClusters* function was performed before manual annotation of clusters based on the expression of canonical gene markers. Smaller clusters and those defined by proliferative markers were subset out and re-clustered alone in order to identify rarer cell types. Statistical analysis of cluster proportions was conducted via a permutation test with 1,000 instances followed by bootstrapping to produce a p-value and confidence interval.

Differential expression: For analysis of differentially expressed genes between conditions, each cluster was filtered to include genes that had at least 5 transcripts in at least 5 cells. The top 2,000 highly variable genes were determined and included for further analysis using the SingleCellExperiment *modelGeneVar* and *getTopHVGs* functions. After filtering, observational weights for each gene were calculated using the ZINB-WaVE *zinbFit* and *zinbwave* functions.[97] These were then included in the edgeR model, which was created with the *glmFit* function by using the *glmWeightedF* function.[98] Results were then filtered using a Benjamini-Hochberg adjusted p-value (adj. p) threshold of less than 0.05 as statistically significant.

Pathway enrichment: Over representation enrichment analysis with Fisher's Exact test was used to determine significantly enriched Gene Ontology (GO) terms (adj. $p < 0.05$) for the sets of significantly differentially expressed genes. For each gene set, genes were separated into up- and down-regulated and separately.[99] The *enrichGO* function from the clusterProfiler package was used with a gene set size set between 10 and 500 genes and p-values adjusted using the Benjamini-Hochberg correction.[100,101]

Macrophage, DC, and monocyte sub-clustering: Cells originally annotated as monocytes, macrophages, or DCs were subset out and were scaled across each gene before the selection of the top 2,000 most highly variable genes using variance stabilizing transformation. Principal Components Analysis was conducted, and an elbow plot was used to select the first twenty principal components for tSNE analysis and clustering. Shared Nearest Neighbor (SNN) clustering optimized with the Louvain algorithm, as implemented by the Seurat *FindClusters* function was performed. Markers defining each subcluster were determined using the Seurat *FindMarkers* function, and genes with an adjusted p-value less than 0.05, positive log fold change, and expression in at least 30 percent of cells were used as input to pathway analysis as described above.

Microglia sub-clustering: Cells originally annotated as microglia were subset out and were scaled across each gene before the selection of the top 2,000 most highly variable genes using variance stabilizing transformation. Principal Components Analysis was conducted, and an elbow plot was used to select the first ten principal components for tSNE analysis and clustering. Shared Nearest Neighbor (SNN) clustering optimized with the Louvain algorithm, as implemented by the Seurat *FindClusters* function was performed. Markers defining each subcluster were determined using the Seurat *FindMarkers* function, and genes with an adjusted p-value less than 0.05, positive log fold change, and expression in at least 30 percent of cells were used as input to pathway analysis as described above. Pseudotime trajectory prediction was performed on the young microglia 3 days post-injury (height of proliferation) using the monocle3 package.[102-106] Specifically, the cells were subset from the Seurat object and converted to a monocle-compatible one. They were pre-processed with *preprocess_cds* function, and the first twelve principal components were determined. The *Mki67* positive cluster was chosen as the starting point to try to identify their transcriptional fate following proliferation.

FACS based single-cell RNA sequencing of meningeal lymphatic endothelial cells—We were unable to capture LECs in meningeal single cell suspension by microfluidics based scRNA-seq method as described above. Therefore, scFACS-seq was used to enrich LECs which have a rare occurrence rate of ~0.5% in the spinal cord meninges.

Cell isolation and sorting: Vertebral columns were obtained after perfusion and cut to include 1 cm around both sides of the lesion site. The ventral bone of the vertebrae was cut laterally and was removed to expose the spinal cord. Nervous tissue was carefully dissected from the bone using fine forceps to release the dorsal root ganglia surrounded by the meninges. The meninges were cut along the ventral side and peeled from the spinal cord. Single cell suspensions of the spinal cord meninges were performed as described above. Cells were resuspended in FACS buffer with 1:100 CD16/32 Fc block. They were stained with CD31, CD45, Podoplanin (PDPN) and LYVE1, washed, and resuspended in DAPI-containing FACS buffer. Single meningeal lymphatic endothelial cells were sorted as viable ($DAPI^-$) $CD45^-$ $CD31^+$ $PDPN^+$ $LYVE1^+$ cells using a FACS Aria II. Individual cells were sorted into 96-well plates containing 2 μL of 10X RNA lysis buffer (Takara) and 5% RNAse out (Takara) and rapidly frozen over dry ice.

FACS-seq: Library preparation was performed with 2 μL of single cell lysates arrayed in 96-well PCR plates. ds-cDNA was prepared using a protocol adapted from the Takara-Clontech SMARTer methods and scaled to a 5 μL reaction volume. This method introduces a unique barcode upstream of the polyA tail using a modified oligo-dT primer. Briefly, 0.5 μL of the Takara dilution buffer with 5% RNase inhibitor and 0.25 μL of 25 μM FACSseq barcode primer was added to the lysate and heated to 72°C for 3 minutes. 2.25 μL of the reverse transcription master mix was added to each well with 1 μL 5X first strand buffer, 0.125 μL 100 mM DTT, 0.25 μL 20 mM dNTPs, 0.25 μL 50 μM FACSseq TSO primer, 0.125 μL RNase inhibitor, and 0.5 μL SMARTscribe reverse transcriptase (Takara). Reaction was incubated at 42°C for 90 minutes, 70°C for 10 minutes, then a 4°C hold. All wells from the plate were then pooled and purified with Ampure XP beads (Beckman Coulter) with a 1X ratio. cDNA was eluted in 39 μL water. cDNA was amplified using 5 μL 10X PCR buffer, 2 μL 10mM dNTPs, 2 μL 12 μM FACSseq TSO PCR primer, 2 μL 50X Advantage 2 Polymerase (Takara). PCR conditions were 95°C for 1 minute, 16 cycles of 95°C for 15 seconds, 65°C for 30 seconds, 68°C for 6 minutes, 1 cycle of 72°C for 10 minutes, followed by a 4°C hold. cDNA was purified with 1.2X Ampure bead cleanup, measured with Qubit dsDNA assay, and visualized on bioanalyzer. cDNA was fragmented using a Covaris E220 sonicator using peak incident power 18, duty factor 20%, cycles per burst 50 for 120 seconds. cDNA was blunt ended, had an A base added to the 3’ ends, and had Illumina sequencing adapters ligated to the ends. Ligated fragments were then amplified for 16 cycles using a standard Illumina i7 primer to introduce an index sequence and FACSseq Lib PCR 1.0 specific to fragments containing the cell barcode added during cDNA synthesis. Fragments were sequenced on an Illumina NextSeq using paired end reads with 25 cycles for read 1, 7 cycles for the i7 index, and 100 cycles for the paired read. The sequencing run was performed with a custom sequencing primer for read 1 to read the 10bp barcode unique to each cell. The i7 index allows for multiple plates to be sequenced together. Read 2 contains the mRNA sequences.

Oligos	Oligo Sequence
FACSseq barcode *	AAGCAGTGGTATCAACGCAGAGTACXXXXXXXXXXTTTTTTTTTTTTTTTTTTTTTTTTTTTTTVN
FACSseq TSO	AAGCAGTGGTATCAACGCAGAGTGAATrGrGrG
FACSseq TSO PCR	AAGCAGTGGTATCAACGCAGAGT
FACSseq Lib PCR 1.0	AATGATACGGCGACCACCGAGATCTACACGCCTGTCCGCGGAAGCAGTGGTATCAACGCAGAGT*A*C
FACSseq Custom Read1	GCCTGTCCGCGGAAGCAGTGGTATCAACGCAGAGTAC

* 10Xs in the FACSseq barcode primer is a 10 nt barcode made up of unique sequences for each sample to be pooled.

Single-cell data preprocessing: Reads were aligned to the mm10 genome using the Cellranger software pipeline (version 6.0.0) provided by 10x genomics. The resulting filtered gene by cell matrix of UMI counts was read into R using the read10xCounts

function from the Droplet Utils package. Expression values for the cells were then processed as described above.

Dimensionality reduction and clustering: The normalized matrix was used as input to the Seurat pipeline, and cells were scaled across each gene before the selection of the top 2,000 most highly variable genes using variance stabilizing transformation. Principal Components Analysis was conducted, and an elbow plot was used to select the first fifteen principal components for tSNE visualization. Cell type identity was verified based on the expression of canonical gene markers.

Ligand-receptor interaction network analysis—Cells from 3 days post injury time points for both young and aged $CD45^+$ sequencing described above were subset and integrated with the injured LEC samples to map possible cell-cell interactions. Possible ligands and receptors were obtained from the annotated reference provided by RNA-Magnet[107] using the *getLigandsReceptors* function with the cellularCompartment parameter set to 'membrane', 'secreted', 'ECM', or 'both' and the version set to 3.0.0. This list was filtered to include ligands that were expressed in at least 20 percent of cells in the myeloid compartment of the CD45+ sequencing and receptors that were expressed in the LEC sequencing. Expression was plotted for cell types of interest as average normalized mRNA transcripts per population with the circlize[108] package in R.

QUANTIFICATION AND STATISTICAL ANALYSIS

Statistical methods were not used to re-calculate or predetermine sample sizes. They were chosen on estimates from previously published experiments. Values are represented as dot plots with individual data points and mean ± SEM as described in the figure legends. *n* indicates the number of animals. The statistical test used to compare two groups is the unpaired two-tailed Mann-Whitney t test. For comparing three or more independent groups, one-way ANOVA with appropriate multiple comparison test (indicated in the figure legend) was used. Statistical tests used for the single-cell RNA sequencing experiments are described in detail in the sections above. A p value of <0.05 is considered statistically significant unless Log_2 fold changes were also considered and are indicated in the figure legends. GraphPad Prism v9.3.0 or R was used for statistical analysis. Experimenters were blinded to the identity of the subjects during tissue harvest and for analysis. To identify outliers in the data, the Grubbs' method was utilized with alpha = 0.05. One outlier was detected and removed in Figure S4K in the naïve control group for quantifications of IFNγ-YFP^+ microglia. For all experiments, animals from different cages were randomly assigned to different experimental groups.

Supplementary Material

Refer to Web version on PubMed Central for supplementary material.

ACKNOWLEDGMENTS

We would like to thank S. Smith for editing the manuscript, Elizabeth Griffin and Abena Apaw for animal care, and Sean Brophy for lab management. We would like to thank the members of the Kipnis lab for their valuable comments during the discussion of this work. We also thank the Genome Technology Access Center at

the McDonnell Genome Institute (MGI) for library preparation and sequencing, and the Flow Cytometry Core of the Department of Pathology and Immunology at the Washington University School of Medicine in St. Louis for assisting with cell sorting. This work was supported by an HHMI Medical Research Fellowship to M.Q.D. and grants from the National Institutes of Health (AT010416, AG034113, NS096967, and AG057496) to J.K.

INCLUSION AND DIVERSITY

We support inclusive, diverse, equitable, and respectful conduct of research.

REFERENCES

1. Badhiwala JH, Wilson JR, and Fehlings MG (2019). Global burden of traumatic brain and spinal cord injury. Lancet Neurol. 18, 24–25. 10.1016/S1474-4422(18)30444-7. [PubMed: 30497967]
2. Popovich PG, Guan Z, Wei P, Huitinga I, van Rooijen N, and Stokes BT (1999). Depletion ofhematogenous macrophages promotes partial hindlimb recovery and neuroanatomical repair after experimental spinal cord injury. Exp. Neurol 158, 351–365. 10.1006/exnr.1999.7118. [PubMed: 10415142]
3. Popovich PG, Stokes BT, and Whitacre CC (1996). Concept of autoimmunity following spinal cord injury: possible roles for T lymphocytes in the traumatized central nervous system. J. Neurosci. Res 45, 349–363. 10.1002/(SICI)1097-4547(19960815)45:4<349::AID-JNR4>3.0.CO;2-9. [PubMed: 8872895]
4. Donnelly DJ, Longbrake EE, Shawler TM, Kigerl KA, Lai W, Tovar CA, Ransohoff RM, and Popovich PG (2011). Deficient CX3CR1 signaling promotes recovery after mouse spinal cord injury by limiting the recruitment and activation of Ly6Clo/iNOS+ macrophages. J. Neurosci 31, 9910–9922. 10.1523/JNEUROSCI.2114-11.2011. [PubMed: 21734283]
5. Gensel JC, Nakamura S, Guan Z, van Rooijen N, Ankeny DP, and Popovich PG (2009). Macrophages promote axon regeneration with concurrent neurotoxicity. J. Neurosci 29, 3956–3968. 10.1523/JNEUROSCI.3992-08.2009. [PubMed: 19321792]
6. Busch SA, Horn KP, Silver DJ, and Silver J (2009). Overcoming macrophage-mediated axonal dieback following CNS injury. J. Neurosci 29, 9967–9976. 10.1523/JNEUROSCI.1151-09.2009. [PubMed: 19675231]
7. Horn KP, Busch SA, Hawthorne AL, van Rooijen N, and Silver J (2008). Another barrier to regeneration in the CNS: activated macrophages induce extensive retraction of dystrophic axons through direct physical interactions. J. Neurosci 28, 9330–9341. 10.1523/JNEUROSCI.2488-08.2008. [PubMed: 18799667]
8. Fawcett JW, and Asher RA (1999). The glial scar and central nervous system repair. Brain Res. Bull 49, 377–391. 10.1016/S0361-9230(99)00072-6. [PubMed: 10483914]
9. Koh TJ, and DiPietro LA (2011). Inflammation and wound healing: the role of the macrophage. Expert Rev. Mol. Med 13, e23. 10.1017/S1462399411001943. [PubMed: 21740602]
10. Schwartz M (2003). Macrophages and microglia in central nervous system injury: are they helpful or harmful? J. Cereb. Blood Flow Metab 23, 385–394. 10.1097/01.WCB.0000061881.75234.5E. [PubMed: 12679714]
11. Raposo C, Graubardt N, Cohen M, Eitan C, London A, Berkutzki T, and Schwartz M (2014). CNS repair requires both effector and regulatory T cells with distinct temporal and spatial profiles. J. Neurosci 34, 10141–10155. 10.1523/JNEUROSCI.0076-14.2014. [PubMed: 25080578]
12. Shechter R, Miller O, Yovel G, Rosenzweig N, London A, Ruckh J, Kim KW, Klein E, Kalchenko V, Bendel P, et al. (2013). Recruitment of beneficial M2 macrophages to injured spinal cord is orchestrated by remote brain choroid plexus. Immunity 38, 555–569. 10.1016/j.immuni.2013.02.012. [PubMed: 23477737]
13. Hauben E, Gothilf A, Cohen A, Butovsky O, Nevo U, Smirnov I, Yoles E, Akselrod S, and Schwartz M (2003). Vaccination with dendritic cells pulsed with peptides of myelin basic protein promotes functional recovery from spinal cord injury. J. Neurosci 23, 8808–8819. [PubMed: 14507981]

14. Hauben E, Nevo U, Yoles E, Moalem G, Agranov E, Mor F, Akselrod S, Neeman M, Cohen IR, and Schwartz M (2000). Autoimmune T cells as potential neuroprotective therapy for spinal cord injury. Lancet 355, 286–287. 10.1016/s0140-6736(99)05140-5. [PubMed: 10675079]
15. Rapalino O, Lazarov-Spiegler O, Agranov E, Velan GJ, Yoles E, Fraidakis M, Solomon A, Gepstein R, Katz A, Belkin M, et al. (1998). Implantation of stimulated homologous macrophages results in partial recovery of paraplegic rats. Nat. Med 4, 814–821. 10.1038/nm0798-814. [PubMed: 9662373]
16. Moalem G, Leibowitz-Amit R, Yoles E, Mor F, Cohen IR, and Schwartz M (1999). Autoimmune T cells protect neurons from secondary degeneration after central nervous system axotomy. Nat. Med 5, 49–55. [PubMed: 9883839]
17. Gaudet AD, Sweet DR, Polinski NK, Guan Z, and Popovich PG (2015). Galectin-1 in injured rat spinal cord: implications for macrophage phagocytosis and neural repair. Mol. Cell. Neurosci 64, 84–94. 10.1016/j.mcn.2014.12.006. [PubMed: 25542813]
18. Greenhalgh AD, and David S (2014). Differences in the phagocytic response of microglia and peripheral macrophages after spinal cord injury and its effects on cell death. J. Neurosci 34, 6316–6322. 10.1523/JNEUROSCI.4912-13.2014. [PubMed: 24790202]
19. Gadani SP, Smirnov I, Wiltbank AT, Overall CC, and Kipnis J (2017). Characterization of meningeal type 2 innate lymphocytes and their response to CNS injury. J. Exp. Med 214, 285–296. 10.1084/jem.20161982. [PubMed: 27994070]
20. Gadani SP, Walsh JT, Lukens JR, and Kipnis J (2015). Dealing with danger in the CNS: the response of the immune system to injury. Neuron 87, 47–62. 10.1016/j.neuron.2015.05.019. [PubMed: 26139369]
21. Shechter R, London A, Varol C, Raposo C, Cusimano M, Yovel G, Rolls A, Mack M, Pluchino S, Martino G, et al. (2009). Infiltrating blood-derived macrophages are vital cells playing an anti-inflammatory role in recovery from spinal cord injury in mice. PLOS Med. 6, e1000113. 10.1371/journal.pmed.1000113. [PubMed: 19636355]
22. Hauben E, Butovsky O, Nevo U, Yoles E, Moalem G, Agranov E, Mor F, Leibowitz-Amit R, Pevsner E, Akselrod S, et al. (2000). Passive or active immunization with myelin basic protein promotes recovery from spinal cord contusion. J. Neurosci 20, 6421–6430. [PubMed: 10964948]
23. Milich LM, Choi JS, Ryan C, Cerqueira SR, Benavides S, Yahn SL, Tsoulfas P, and Lee JK (2021). Single-cell analysis of the cellular heterogeneity and interactions in the injured mouse spinal cord. J. Exp. Med 218, e20210040. 10.1084/jem.20210040. [PubMed: 34132743]
24. Wahane S, Zhou X, Zhou X, Guo L, Friedl M-S, Kluge M, Ramakrishnan A, Shen L, Friedel CC, Zhang B, et al. (2021). Diversified transcriptional responses of myeloid and glial cells in spinal cord injury shaped by HDAC3 activity. Sci. Adv 7, eabd8811. 10.1126/sciadv.abd8811. [PubMed: 33637528]
25. Plemel JR, Stratton JA, Michaels NJ, Rawji KS, Zhang E, Sinha S, Baaklini CS, Dong Y, Ho M, Thorburn K, et al. (2020). Microglia response following acute demyelination is heterogeneous and limits infiltrating macrophage dispersion. Sci. Adv 6, eaay6324. 10.1126/sciadv.aay6324. [PubMed: 31998844]
26. Hakim R, Zachariadis V, Sankavaram SR, Han J, Harris RA, Brundin L, Enge M, and Svensson M (2021). Spinal cord injury induces permanent reprogramming of microglia into a disease-associated state which contributes to functional recovery. J. Neurosci 41, 8441–8459. 10.1523/JNEUROSCI.0860-21.2021. [PubMed: 34417326]
27. Brennan FH, Li Y, Wang C, Ma A, Guo Q, Li Y, Pukos N, Campbell WA, Witcher KG, Guan Z, et al. (2022). Microglia coordinate cellular interactions during spinal cord repair in mice. Nat. Commun 13, 4096. 10.1038/s41467-022-31797-0. [PubMed: 35835751]
28. Li Y, He X, Kawaguchi R, Zhang Y, Wang Q, Monavarfeshani A, Yang Z, Chen B, Shi Z, Meng H, et al. (2020). Microglia-organized scar-free spinal cord repair in neonatal mice. Nature 587, 613–618. [PubMed: 33029008]
29. Bellver-Landete V, Bretheau F, Mailhot B, Vallières N, Lessard M, Janelle M-È, Vernoux N, Tremblay M-E, Fuehrmann T, Shoichet MS, and Lacroix S (2019). Microglia are an essential component of the neuroprotective scar that forms after spinal cord injury. Nat. Commun 10, 518. 10.1038/s41467-019-08446-0. [PubMed: 30705270]

30. Alves de Lima K, Rustenhoven J, and Kipnis J (2020). Meningeal immunity and its function in maintenance of the central nervous system in health and disease. Annu. Rev. Immunol 38, 597–620. 10.1146/annurev-immunol-102319-103410. [PubMed: 32340575]

31. Rustenhoven J, and Kipnis J (2022). Brain borders at the central stage of neuroimmunology. Nature 612, 417–429. 10.1038/s41586-022-05474-7. [PubMed: 36517712]

32. Aspelund A, Antila S, Proulx ST, Karlsen TV, Karaman S, Detmar M, Wiig H, and Alitalo K (2015).A dural lymphatic vascular system that drains brain interstitial fluid and macromolecules. J. Exp. Med 212, 991–999. 10.1084/jem.20142290. [PubMed: 26077718]

33. Louveau A, Smirnov I, Keyes TJ, Eccles JD, Rouhani SJ, Peske JD, Derecki NC, Castle D, Mandell JW, Lee KS, et al. (2015). Structural and functional features of central nervous system lymphatic vessels. Nature 523, 337–341. 10.1038/nature14432. [PubMed: 26030524]

34. Rustenhoven J, Drieu A, Mamuladze T, de Lima KA, Dykstra T, Wall M, Papadopoulos Z, Kanamori M, Salvador AF, Baker W, et al. (2021). Functional characterization ofthe dural sinuses as a neuro-immune interface. Cell 184, 1000–1016.e27. 10.1016/j.cell.2020.12.040. [PubMed: 33508229]

35. Mrdjen D, Pavlovic A, Hartmann FJ, Schreiner B, Utz SG, Leung BP, Lelios I, Heppner FL, Kipnis J, Merkler D, et al. (2018). High-dimensional single-cell mapping of central nervous system immune cells reveals distinct myeloid subsets in health, aging, and disease. Immunity 48, 380–395.e6. 10.1016/j.immuni.2018.01.011. [PubMed: 29426702]

36. Da Mesquita S, Papadopoulos Z, Dykstra T, Brase L, Farias FG, Wall M, Jiang H, Kodira CD, de Lima KA, Herz J, et al. (2021). Meningeal lymphatics affect microglia responses and anti-Aβ immunotherapy. Nature 593, 255–260. 10.1038/s41586-021-03489-0. [PubMed: 33911285]

37. Louveau A, Herz J, Alme MN, Salvador AF, Dong MQ, Viar KE, Herod SG, Knopp J, Setliff JC, Lupi AL, et al. (2018). CNS lymphatic drainage and neuroinflammation are regulated by meningeal lymphatic vasculature. Nat. Neurosci 21, 1380–1391. 10.1038/s41593-018-0227-9. [PubMed: 30224810]

38. Song E, Mao T, Dong H, Boisserand LSB, Antila S, Bosenberg M, Alitalo K, Thomas JL, and Iwasaki A (2020). VEGF-C-driven lymphatic drainage enables immunosurveillance of brain tumours. Nature 577, 689–694. 10.1038/s41586-019-1912-x. [PubMed: 31942068]

39. Hu X, Deng Q, Ma L, Li Q, Chen Y, Liao Y, Zhou F, Zhang C, Shao L, Feng J, et al. (2020). Meningeal lymphatic vessels regulate brain tumor drainage and immunity. Cell Res. 30, 229–243. 10.1038/s41422-020-0287-8. [PubMed: 32094452]

40. Takano M, Kawabata S, Shibata S, Yasuda A, Nori S, Tsuji O, Nagoshi N, Iwanami A, Ebise H, Horiuchi K, et al. (2017). Enhanced functional recovery from spinal cord injury in aged mice after stem cell transplantation through HGF induction. Stem Cell Rep. 8, 509–518. 10.1016/j.stemcr.2017.01.013.

41. Siegenthaler MM, Ammon DL, and Keirstead HS (2008). Myelin pathogenesis and functional deficits following SCI are age-associated. Exp. Neurol 213, 363–371. 10.1016/j.expneurol.2008.06.015. [PubMed: 18644369]

42. Ritzel RM, Crapser J, Patel AR, Verma R, Grenier JM, Chauhan A, Jellison ER, and McCullough LD (2016). Age-associated resident memory CD8 T cells in the central nervous system are primed to potentiate inflammation after ischemic brain injury. J. Immunol 196, 3318–3330. 10.4049/jimmunol.1502021. [PubMed: 26962232]

43. Dulken BW, Buckley MT, Navarro Negredo P, Saligrama N, Cayrol R, Leeman DS, George BM, Boutet SC, Hebestreit K, Pluvinage JV, et al. (2019). Single-cell analysis reveals T cell infiltration in old neurogenic niches. Nature 571, 205–210. 10.1038/s41586-019-1362-5. [PubMed: 31270459]

44. Oja AE, van Lier RAW, and Hombrink P (2022). Two sides of the same coin: protective versus pathogenic CD4+ resident memory T cells. Sci. Immunol 7, eabf9393. 10.1126/sciimmunol.abf9393. [PubMed: 35394815]

45. Castellino F, Huang AY, Altan-Bonnet G, Stoll S, Scheinecker C, and Germain RN (2006). Chemokines enhance immunity by guiding naive CD8+ T cells to sites of CD4+ T cell-dendritic cell interaction. Nature 440, 890–895. 10.1038/nature04651. [PubMed: 16612374]

46. Kigerl KA, Gensel JC, Ankeny DP, Alexander JK, Donnelly DJ, and Popovich PG (2009). Identification of two distinct macrophage subsets with divergent effects causing either neurotoxicity or regeneration in the injured mouse spinal cord. J. Neurosci 29, 13435–13444. 10.1523/JNEUROSCI.3257-09.2009. [PubMed: 19864556]
47. Van Hove H, Martens L, Scheyltjens I, De Vlaminck K, Pombo Antunes AR, De Prijck S, Vandamme N, De Schepper S, Van Isterdael G, Scott CL, et al. (2019). A single-cell atlas of mouse brain macrophages reveals unique transcriptional identities shaped by ontogeny and tissue environment. Nat. Neurosci 22, 1021–1035. [PubMed: 31061494]
48. Drieu A, Du S, Storck SE, Rustenhoven J, Papadopoulos Z, Dykstra T, Zhong F, Kim K, Blackburn S, Mamuladze T, et al. (2022). Parenchymal border macrophages regulate the flow dynamics of the cerebrospinal fluid. Nature 611, 585–593. 10.1038/s41586-022-05397-3. [PubMed: 36352225]
49. Hammond TR, Dufort C, Dissing-Olesen L, Giera S, Young A, Wysoker A, Walker AJ, Gergits F, Segel M, Nemesh J, et al. (2019). Single-cell RNA sequencing of microglia throughout the mouse lifespan and in the injured brain reveals complex cell-state changes. Immunity 50, 253–271.e6. 10.1016/j.immuni.2018.11.004. [PubMed: 30471926]
50. Mathys H, Adaikkan C, Gao F, Young JZ, Manet E, Hemberg M, De Jager PL, Ransohoff RM, Regev A, and Tsai L-H (2017). Temporal tracking of microglia activation in neurodegeneration at single-cell resolution. Cell Rep. 21, 366–380. 10.1016/j.cel-rep.2017.09.039. [PubMed: 29020624]
51. Friedman BA, Srinivasan K, Ayalon G, Meilandt WJ, Lin H, Huntley MA, Cao Y, Lee SH, Haddick PCG, Ngu H, et al. (2018). Diverse brain myeloid expression profiles reveal distinct microglial activation states and aspects of Alzheimer's disease not evident in mouse models. Cell Rep. 22, 832–847. 10.1016/j.celrep.2017.12.066. [PubMed: 29346778]
52. Paolicelli RC, Sierra A, Stevens B, Tremblay M-E, Aguzzi A, Ajami B, Amit I, Audinat E, Bechmann I, Bennett M, et al. (2022). Microglia states and nomenclature: A field at its crossroads. Neuron 110, 3458–3483. 10.1016/j.neuron.2022.10.020. [PubMed: 36327895]
53. Keren-Shaul H, Spinrad A, Weiner A, Matcovitch-Natan O, Dvir-Szternfeld R, Ulland TK, David E, Baruch K, Lara-Astaiso D, Toth B, et al. (2017). A unique microglia type associated with restricting development of Alzheimer's disease. Cell 169, 1276–1290.e17. 10.1016/j.cell.2017.05.018. [PubMed: 28602351]
54. Krasemann S, Madore C, Cialic R, Baufeld C, Calcagno N, El Fatimy R, Beckers L, O'Loughlin E, Xu Y, Fanek Z, et al. (2017). The TREM2-APOE pathway drives the transcriptional phenotype of dysfunctional microglia in neurodegenerative diseases. Immunity 47, 566–581.e9. 10.1016/j.immuni.2017.08.008. [PubMed: 28930663]
55. Saul D, Kosinsky RL, Atkinson EJ, Doolittle ML, Zhang X, LeBrasseur NK, Pignolo RJ, Robbins PD, Niedernhofer LJ, Ikeno Y, et al. (2022). A new gene set identifies senescent cells and predicts senescence-associated pathways across tissues. Nat. Commun 13, 4827. 10.1038/s41467-022-32552-1. [PubMed: 35974106]
56. Basso DM, Fisher LC, Anderson AJ, Jakeman LB, McTigue DM, and Popovich PG (2006). Basso Mouse Scale for locomotion detects differences in recovery after spinal cord injury in five common mouse strains. J. Neurotrauma 23, 635–659. 10.1089/neu.2006.23.635. [PubMed: 16689667]
57. Scheu S, Dresing P, and Locksley RM (2008). Visualization of IFNbeta production by plasmacytoid versus conventional dendritic cells under specific stimulation conditions in vivo. Proc. Natl. Acad. Sci. USA 105, 20416–20421. 10.1073/pnas.0808537105. [PubMed: 19088190]
58. Reinhardt RL, Liang H-E, and Locksley RM (2009). Cytokine-secreting follicular T cells shape the antibody repertoire. Nat. Immunol 10, 385–393. 10.1038/ni.1715. [PubMed: 19252490]
59. Zhu Y, Lyapichev K, Lee DH, Motti D, Ferraro NM, Zhang Y, Yahn S, Soderblom C, Zha J, Bethea JR, et al. (2017). Macrophage transcriptional profile identifies lipid catabolic pathways that can be therapeutically targeted after spinal cord injury. J. Neurosci 37, 2362–2376. 10.1523/JNEUROSa.2751-16.2017. [PubMed: 28130359]
60. Atabai K, Jame S, Azhar N, Kuo A, Lam M, McKleroy W, Dehart G, Rahman S, Xia DD, Melton AC, et al. (2009). Mfge8 diminishes the severity of tissue fibrosis in mice by binding and targeting collagen for uptake by macrophages. J. Clin. Invest 119, 3713–3722. 10.1172/JCI40053. [PubMed: 19884654]

61. Kandalam V, Basu R, Abraham T, Wang X, Soloway PD, Jaworski DM, Oudit GY, and Kassiri Z (2010). TIMP2 deficiency accelerates adverse post-myocardial infarction remodeling because of enhanced MT1-MMP activity despite lack of MMP2 activation. Circ. Res 106, 796–808. 10.1161/CIRCRESAHA.109.209189. [PubMed: 20056917]
62. Mastorakos P, Mihelson N, Luby M, Burks SR, Johnson K, Hsia AW, Witko J, Frank JA, Latour L, and McGavern DB (2021). Temporally distinct myeloid cell responses mediate damage and repair after cerebrovascular injury. Nat. Neurosci 24, 245–258. 10.1038/s41593-020-00773-6. [PubMed: 33462481]
63. Jacob L, Boisserand LSB, Geraldo LHM, de Brito Neto J, Mathivet T, Antila S, Barka B, Xu Y, Thomas J-M, Pestel J, et al. (2019). Anatomy and function of the vertebral column lymphatic network in mice. Nat. Commun 10, 4594. 10.1038/s41467-019-12568-w. [PubMed: 31597914]
64. Cao Y, Linden P, Farnebo J, Cao R, Eriksson A, Kumar V, Qi JH, Claesson-Welsh L, and Alitalo K (1998). Vascular endothelial growth factor C induces angiogenesis in vivo. Proc. Natl. Acad. Sci. USA 95, 14389–14394. 10.1073/pnas.95.24.14389. [PubMed: 9826710]
65. Jeltsch M, Kaipainen A, Joukov V, Meng X, Lakso M, Rauvala H, Swartz M, Fukumura D, Jain RK, and Alitalo K (1997). Hyperplasia of lymphatic vessels in VEGF-C transgenic mice. Science 276, 1423–1425. 10.1126/science.276.5317.1423. [PubMed: 9162011]
66. Antila S, Karaman S, Nurmi H, Airavaara M, Voutilainen MH, Mathivet T, Chilov D, Li Z, Koppinen T, Park JH, et al. (2017). Development and plasticity of meningeal lymphatic vessels. J. Exp. Med 214, 3645–3667. 10.1084/jem.20170391. [PubMed: 29141865]
67. Von Korff M, Crane P, Lane M, Miglioretti DL, Simon G, Saunders K, Stang P, Brandenburg N, and Kessler R (2005). Chronic spinal pain and physical-mental comorbidity in the United States: results from the national comorbidity survey replication. Pain 113, 331–339. 10.1016/j.pain.2004.11.010. [PubMed: 15661441]
68. Yezierski RP (2012). The effects of age on pain sensitivity: preclinical studies. Pain Med. 13, S27–S36. 10.1111/j.1526-4637.2011.01311.x. [PubMed: 22497745]
69. Kim H, Kataru RP, and Koh GY (2014). Inflammation-associated lymphangiogenesis: a double-edged sword? J. Clin. Invest 124, 936–942. [PubMed: 24590279]
70. Brubaker AL, Rendon JL, Ramirez L, Choudhry MA, and Kovacs EJ (2013). Reduced neutrophil chemotaxis and infiltration contributes to delayed resolution of cutaneous wound infection with advanced age. J. Immunol 190, 1746–1757. 10.4049/jimmunol.1201213. [PubMed: 23319733]
71. Greenhalgh AD, Zarruk JG, Healy LM, Baskar Jesudasan SJ, Jhelum P, Salmon CK, Formanek A, Russo MV, Antel JP, McGavern DB, et al. (2018). Peripherally derived macrophages modulate microglial function to reduce inflammation after CNS injury. PLoS Biol. 16, e2005264. 10.1371/journal.pbio.2005264. [PubMed: 30332405]
72. Nahrendorf M, Swirski FK, Aikawa E, Stangenberg L, Wurdinger T, Figueiredo J-L, Libby P, Weissleder R, and Pittet MJ (2007). The healing myocardium sequentially mobilizes two monocyte subsets with divergent and complementary functions. J. Exp. Med 204, 3037–3047. 10.1084/jem.20070885. [PubMed: 18025128]
73. Cugurra A, Mamuladze T, Rustenhoven J, Dykstra T, Beroshvili G, Greenberg ZJ, Baker W, Papadopoulos Z, Drieu A, Blackburn S, et al. (2021). Skull and vertebral bone marrow are myeloid cell reservoirs forthe meninges and CNS parenchyma. Science 373, eabf7844. 10.1126/science.abf7844. [PubMed: 34083447]
74. Mazzitelli JA, Smyth LCD, Cross KA, Dykstra T, Sun J, Du S, Mamuladze T, Smirnov I, Rustenhoven J, and Kipnis J (2022). Cerebrospinal fluid regulates skull bone marrow niches via direct access through dural channels. Nat. Neurosci 25, 555–560. 10.1038/s41593-022-01029-1. [PubMed: 35301477]
75. Herisson F, Frodermann V, Courties G, Rohde D, Sun Y, Vandoorne K, Wojtkiewicz GR, Masson GS, Vinegoni C, Kim J, et al. (2018). Direct vascular channels connect skull bone marrow and the brain surface enabling myeloid cell migration. Nat. Neurosci 21, 1209–1217. 10.1038/s41593-018-0213-2. [PubMed: 30150661]
76. Yao H, Price TT, Cantelli G, Ngo B, Warner MJ, Olivere L, Ridge SM, Jablonski EM, Therrien J, Tannheimer S, et al. (2018). Leukaemia hijacks a neural mechanism to invade the central nervous system. Nature 560, 55–60. 10.1038/s41586-018-0342-5. [PubMed: 30022166]

77. Wichmann TO, Damkier HH, and Pedersen M (2021). A brief overview of the cerebrospinal fluid system and its implications for brain and spinal cord diseases. Front. Hum. Neurosci 15, 737217. 10.3389/fnhum.2021.737217. [PubMed: 35126070]

78. Zhang B, Bailey WM, McVicar AL, Stewart AN, Veldhorst AK, and Gensel JC (2019). Reducing age-dependent monocyte-derived macrophage activation contributes to the therapeutic efficacy of NADPH oxidase inhibition in spinal cord injury. Brain Behav. Immun 76, 139–150. 10.1016/j.bbi.2018.11.013. [PubMed: 30453022]

79. Deczkowska A, Keren-Shaul H, Weiner A, Colonna M, Schwartz M, and Amit I (2018). Disease-associated microglia: A universal immune sensor of neurodegeneration. Cell 173, 1073–1081. 10.1016/j.cell.2018.05.003. [PubMed: 29775591]

80. Matson KJE, Russ DE, Kathe C, Hua I, Maric D, Ding Y, Krynitsky J, Pursley R, Sathyamurthy A, Squair JW, et al. (2022). Single cell atlas of spinal cord injury in mice reveals a pro-regenerative signature in spinocerebellar neurons. Nat. Commun 13, 5628. 10.1038/s41467-022-33184-1. [PubMed: 36163250]

81. Wang Y, Cella M, Mallinson K, Ulrich JD, Young KL, Robinette ML, Gilfillan S, Krishnan GM, Sudhakar S, Zinselmeyer BH, et al. (2015). TREM2 lipid sensing sustains the microglial response in an Alzheimer's disease model. Cell 160, 1061–1071. 10.1016/j.cell.2015.01.049. [PubMed: 25728668]

82. Gratuze M, Chen Y, Parhizkar S, Jain N, Strickland MR, Serrano JR, Colonna M, Ulrich JD, and Holtzman DM (2021). Activated microglia mitigate Aβ-associated tau seeding and spreading. J. Exp. Med 218, e20210542. 10.1084/jem.20210542. [PubMed: 34100905]

83. Ennerfelt H, Frost EL, Shapiro DA, Holliday C, Zengeler KE, Voithofer G, Bolte AC, Lammert CR, Kulas JA, Ulland TK, and Lukens JR (2022). SYK coordinates neuroprotective microglial responses in neurodegenerative disease. Cell 185, 4135–4152.e22. 10.1016/j.cell.2022.09.030. [PubMed: 36257314]

84. Wang S, Sudan R, Peng V, Zhou Y, Du S, Yuede CM, Lei T, Hou J, Cai Z, Cella M, et al. (2022). TREM2 drives microglia response to amyloid-β via SYK-dependent and -independent pathways. Cell 185, 4153–169.e19. 10.1016/j.cell.2022.09.033. [PubMed: 36306735]

85. Marrack P, Kappler J, and Mitchell T (1999). Type I interferons keep activated T cells alive. J. Exp. Med 189, 521–530. 10.1084/jem.189.3.521. [PubMed: 9927514]

86. Benakis C, Simats A, Tritschler S, Heindl S, Besson-Girard S, Llovera G, Pinkham K, Kolz A, Ricci A, Theis FJ, et al. (2022). T cells modulate the microglial response to brain ischemia. eLife 11, e82031. 10.7554/eLife.82031. [PubMed: 36512388]

87. Burns JC, Cotleur B, Walther DM, Bajrami B, Rubino SJ, Wei R, Franchimont N, Cotman SL, Ransohoff RM, and Mingueneau M (2020). Differential accumulation of storage bodies with aging defines discrete subsets of microglia in the healthy brain. eLife 9, e57495. 10.7554/eLife.57495. [PubMed: 32579115]

88. Yao C, Cao X, and Yu B (2021). Revascularization aftertraumatic spinal cord injury. Front. Physiol 12, 631500. 10.3389/fphys.2021.631500. [PubMed: 33995118]

89. Bolte AC, Shapiro DA, Dutta AB, Ma WF, Bruch KR, Kovacs MA, Royo Marco A, Ennerfelt HE, and Lukens JR (2023). The meningeal transcriptional response to traumatic brain injury and aging. eLife 12, e81154. 10.7554/eLife.81154. [PubMed: 36594818]

90. Shimizu Y, Polavarapu R, Eskla KL, Pantner Y, Nicholson CK, Ishii M, Brunnhoelzl D, Mauria R, Husain A, Naqvi N, et al. (2018). Impact of lymphangiogenesis on cardiac remodeling after ischemia and reperfusion injury. J. Am. Heart Assoc 7, e009565. 10.1161/JAHA.118.009565. [PubMed: 30371303]

91. Zhou Y, Song WM, Andhey PS, Swain A, Levy T, Miller KR, Poliani PL, Cominelli M, Grover S, Gilfillan S, et al. (2020). Human and mouse single-nucleus transcriptomics reveal TREM2-dependent and TREM2-independent cellular responses in Alzheimer's disease. Nat. Med 26, 131–142. 10.1038/s41591-019-0695-9. [PubMed: 31932797]

92. Chen Z, Raj A, Prateek GV, Di Francesco A, Liu J, Keyes BE, Kolumam G, Jojic V, and Freund A (2022). Automated, high-dimensional evaluation of physiological aging and resilience in outbred mice. eLife 11, e72664. 10.7554/eLife.72664. [PubMed: 35404230]

93. Schneider CA, Rasband WS, and Eliceiri KW (2012). NIH Image to ImageJ: 25 years of image analysis. Nat. Methods 9, 671–675. 10.1038/nmeth.2089. [PubMed: 22930834]

94. Butler A, Hoffman P, Smibert P, Papalexi E, and Satija R (2018). Integrating single-cell transcriptomic data across different conditions, technologies, and species. Nat. Biotechnol 36, 411–420. 10.1038/nbt.4096. [PubMed: 29608179]

95. Lun ATL, McCarthy DJ, and Marioni JC (2016). A step-by-step workflow for low-level analysis of single-cell RNA-seq data with Bioconductor. F1000Res 5, 2122. 10.12688/f1000research.9501.2. [PubMed: 27909575]

96. McCarthy DJ, Campbell KR, Lun ATL, and Wills QF (2017). Scater: pre-processing, quality control, normalization and visualization of single-cell RNA-seq data in R. Bioinformatics 33, 1179–1186. 10.1093/bioinformatics/btw777. [PubMed: 28088763]

97. Van den Berge K, Perraudeau F, Soneson C, Love MI, Risso D, Vert J-P, Robinson MD, Dudoit S, and Clement L (2018). Observation weights unlock bulk RNA-seq tools for zero inflation and single-cell applications. Genome Biol. 19, 24. 10.1186/s13059-018-1406-4. [PubMed: 29478411]

98. Robinson MD, McCarthy DJ, and Smyth GK (2010). edgeR: a Bioconductor package for differential expression analysis of digital gene expression data. Bioinformatics 26, 139–140. 10.1093/bioinformatics/btp616. [PubMed: 19910308]

99. Hong G, Zhang W, Li H, Shen X, and Guo Z (2014). Separate enrichment analysis of pathways for up- and downregulated genes. J. R. Soc. Interface 11, 20130950. 10.1098/rsif.2013.0950. [PubMed: 24352673]

100. Yu G, Wang L-G, Yan G-R, and He Q-Y (2015). DOSE: an R/Bioconductor package for disease ontology semantic and enrichment analysis. Bioinformatics 31, 608–609. 10.1093/bioinformatics/btu684. [PubMed: 25677125]

101. Yu G, Wang L-G, Han Y, and He Q-Y (2012). clusterProfiler: an R package for comparing biological themes among gene clusters. Omics 16, 284–287. 10.1089/omi.2011.0118. [PubMed: 22455463]

102. Cao J, Spielmann M, Qiu X, Huang X, Ibrahim DM, Hill AJ, Zhang F, Mundlos S, Christiansen L, Steemers FJ, et al. (2019). The single-cell transcriptional landscape of mammalian organogenesis. Nature 566, 496–502. 10.1038/s41586-019-0969-x. [PubMed: 30787437]

103. Qiu X, Mao Q, Tang Y, Wang L, Chawla R, Pliner HA, and Trapnell C (2017). Reversed graph embedding resolves complex single-cell trajectories. Nat. Methods 14, 979–982. 10.1038/nmeth.4402. [PubMed: 28825705]

104. Trapnell C, Cacchiarelli D, Grimsby J, Pokharel P, Li S, Morse M, Lennon NJ, Livak KJ, Mikkelsen TS, and Rinn JL (2014). The dynamics and regulators of cell fate decisions are revealed by pseudotemporal ordering of single cells. Nat. Biotechnol 32, 381–386. 10.1038/nbt.2859. [PubMed: 24658644]

105. Traag VA, Waltman L, and van Eck NJ (2019). From Louvain to Leiden: guaranteeing well-connected communities. Sci. Rep 9, 5233. 10.1038/s41598-019-41695-z. [PubMed: 30914743]

106. Levine JH, Simonds EF, Bendall SC, Davis KL, Amir E.-a.D., Tadmor MD, Litvin O, Fienberg HG, Jager A, Zunder ER, et al. (2015). Data-driven phenotypic dissection of AML reveals progenitor-like cells that correlate with prognosis. Cell 162, 184–197. 10.1016/j.cell.2015.05.047. [PubMed: 26095251]

107. Baccin C, Al-Sabah J, Velten L, Helbling PM, Grünschläger F, Hernández-Malmierca P, Nombela-Arrieta C, Steinmetz LM, Trumpp A, and Haas S (2020). Combined single-cell and spatial transcriptomics reveal the molecular, cellular and spatial bone marrow niche organization. Nat. Cell Biol 22, 38–48. 10.1038/s41556-019-0439-6. [PubMed: 31871321]

108. Gu Z, Gu L, Eils R, Schlesner M, and Brors B (2014). circlize Implements and enhances circular visualization in R. Bioinformatics 30, 2811–2812. 10.1093/bioinformatics/btu393. [PubMed: 24930139]

Highlights

- scRNA-seq reveals age-related immune cell responses after SCI
- Myeloid cell infiltration and diversification is impaired in aged mice after SCI
- A subset of microglia in aged mice displays deficits at steady state and after SCI
- Parenchymal and meningeal myeloid cells facilitate injury-related lymphangiogenesis

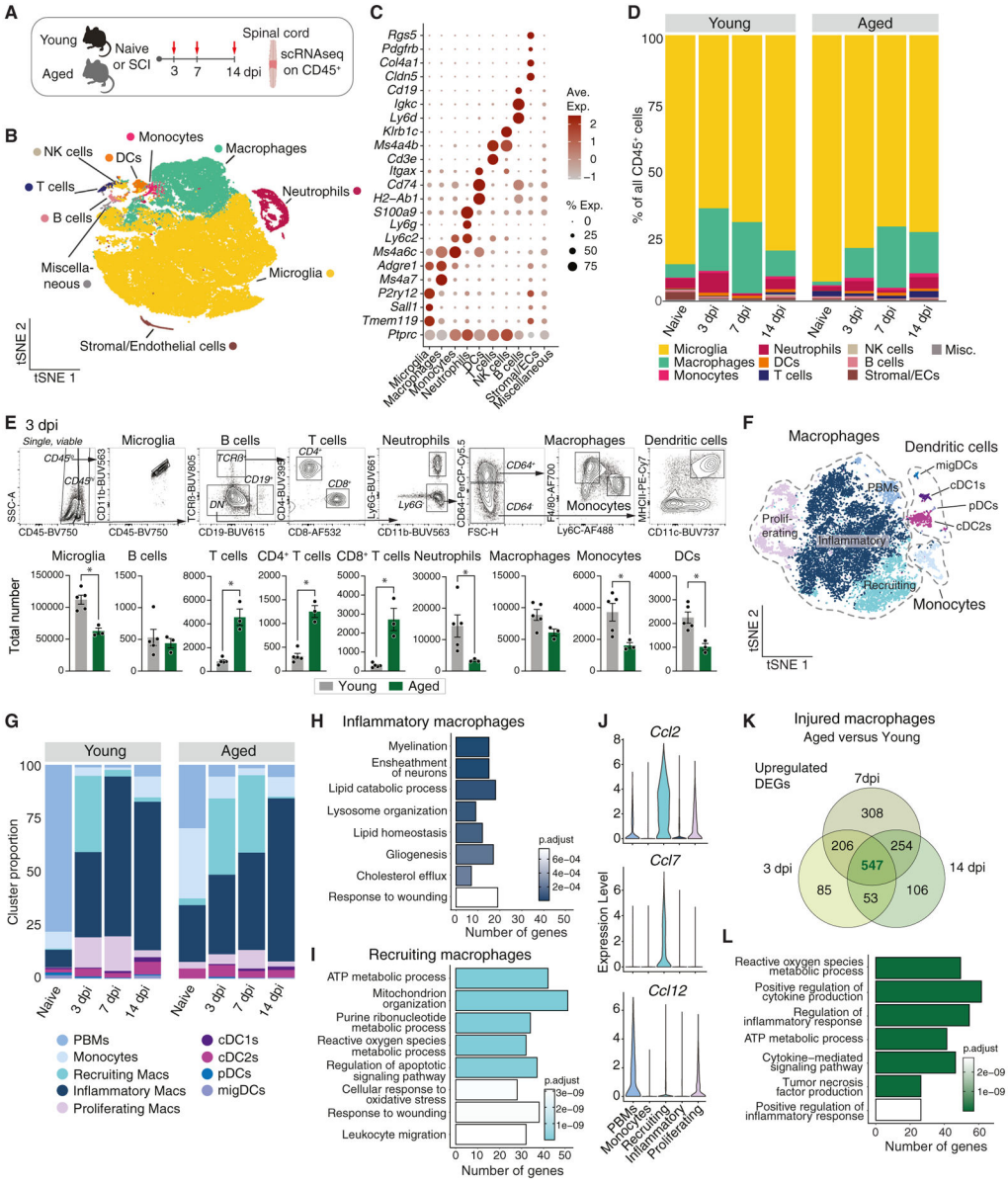

Figure 1. Aging leads to an altered myeloid cell recruitment and increased chemokine induction in macrophages after spinal cord contusion injury

(A) Young (2–3 months old) and aged (20–24 months old) female C57BL/6 mice were subjected to spinal cord contusion injury at T9 and compared to naive mice. $CD45^+$ cells were enriched immunomagnetically 3, 7, and 14 days post injury (dpi) from the spinal cord lesion site (spinal cord and leptomeninges) and then subjected to single-cell RNA sequencing (scRNA-seq).

(B) t-distributed stochastic neighbor embedding (tSNE) visualization of scRNA-seq analysis of the $CD45^+$ populations from spinal cords of young and aged mice. Colors correspond to clustering of immune cell populations. n = 5 mice pooled for all young samples, 7 and 14 dpi aged, n = 3 mice pooled for aged naive and 3 dpi. DCs, dendritic cells.

(C) Scaled average gene expression and percentage of cells expressing phenotyping markers for each population.

(D) Proportions of spinal cord leukocytes in naive and injured spinal cords from young and aged mice. ECs, endothelial cells; Misc., miscellaneous.

(E) Flow cytometric assessment and quantification of the total number of cells in the spinal cord of young and aged mice at 3 dpi. Each dot represents an individual mouse. n = 5 young and 3 aged mice. Data are presented as mean ± SEM. Significance was determined using Mann-Whitney test, *$p < 0.05$.

(F) tSNE visualization after re-clustering of selected myeloid cell populations (macrophages, monocytes, and DCs) shown in (A).

(G) Proportions of myeloid cell types in naive and injured spinal cords of young and aged mice.

(H and I) Gene ontology (GO) terms associated with upregulated gene markers for (H) inflammatory and (I) recruiting macrophages.

(J) Violin plots showing normalized expression of *Ccl2*, *Ccl7*, and *Ccl12* across monocyte and macrophage clusters.

(K) Venn diagram comparing upregulated DEGs between macrophage populations from aged and young mice for each injury time point.

(L) GO pathway analysis demonstrating enriched pathways in injured macrophages between the shared DEGs described in (K).

See also Figures S1-S3 and Tables S1, S2, S3, S4, and S5.

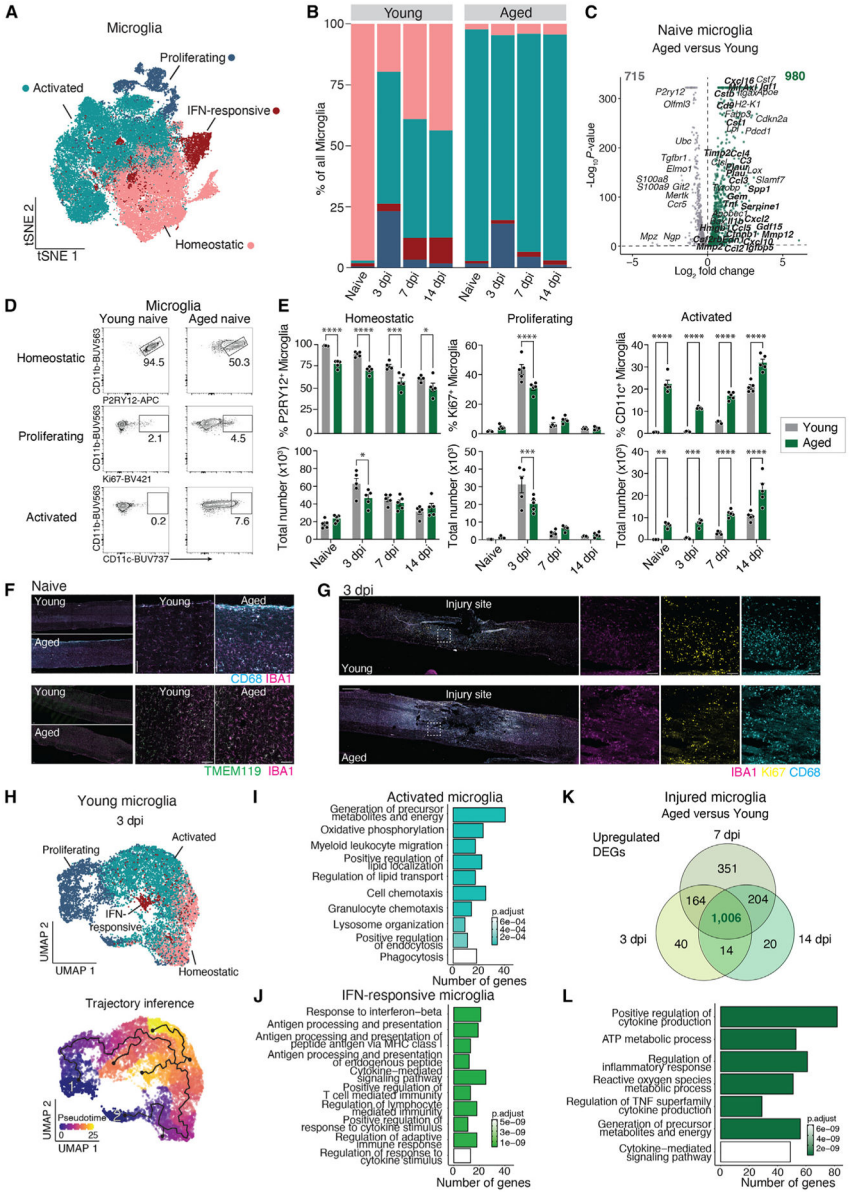

Figure 2. Microglia in the aged spinal cord display an extended activated state and have reduced potential to transition to other microglial populations after injury

(A) tSNE visualization of microglia subclustered from scRNA-seq analysis of young and aged female mice shown in Figures 1A-1D.

(B) Cluster distributions of microglia in young and aged mice that were naive or 3, 7, and 14 days post-spinal cord injury (dpi).

(C) Volcano plot showing differentially expressed genes between microglia from naive spinal cords in aged and young mice. Genes in bold text represent senescent-related genes identified in the SenMayo[55] dataset.

(D and E) (D) Flow cytometric assessment and (E) quantification of frequencies and total numbers of microglia in young and aged spinal cords (spinal cord and leptomeninges) at multiple time points after injury. Each dot represents an individual mouse. n = 5 mice per group. Data are presented as mean ± SEM. Significance was determined using two-way

ANOVA with multiple comparisons and Sidak's post hoc test, *p < 0.05, **p < 0.01, ***p < 0.001, and ****p < 0.0001.

(F and G) (F) Immunohistochemistry of activated microglia ($CD68^+$ $IBA1^+$) and homeostatic microglia ($TMEM119^+$ $IBA1^+$) in the spinal cord of naive young and aged animals, and (G) proliferating microglia ($Ki67^+$ $IBA1^+$), 3 days post injury. Representative micrographs of n = 2 naive and n = 3 injured mice. Scale bars, 500 and 100 μm.

(H) Inferred differentiation trajectory of proliferating microglia obtained from young mice 3 dpi, using pseudotime analysis and visualized in a uniform manifold approximation and projection (UMAP). The numbered clusters (1) and (2) represent starting points of the predicted trajectory.

(I and J) Gene ontology (GO) terms associated with the marker genes of (I) activated microglia and (J) interferon (IFN)-responsive microglia in injured mice.

(K) Venn diagram showing the overlap of upregulated DEGs found between aged versus young microglia across all injury time points.

(L) GO terms describing the overlap between the upregulated DEGs described in (K).

See also Figure S4 and Tables S3, S4, and S5.

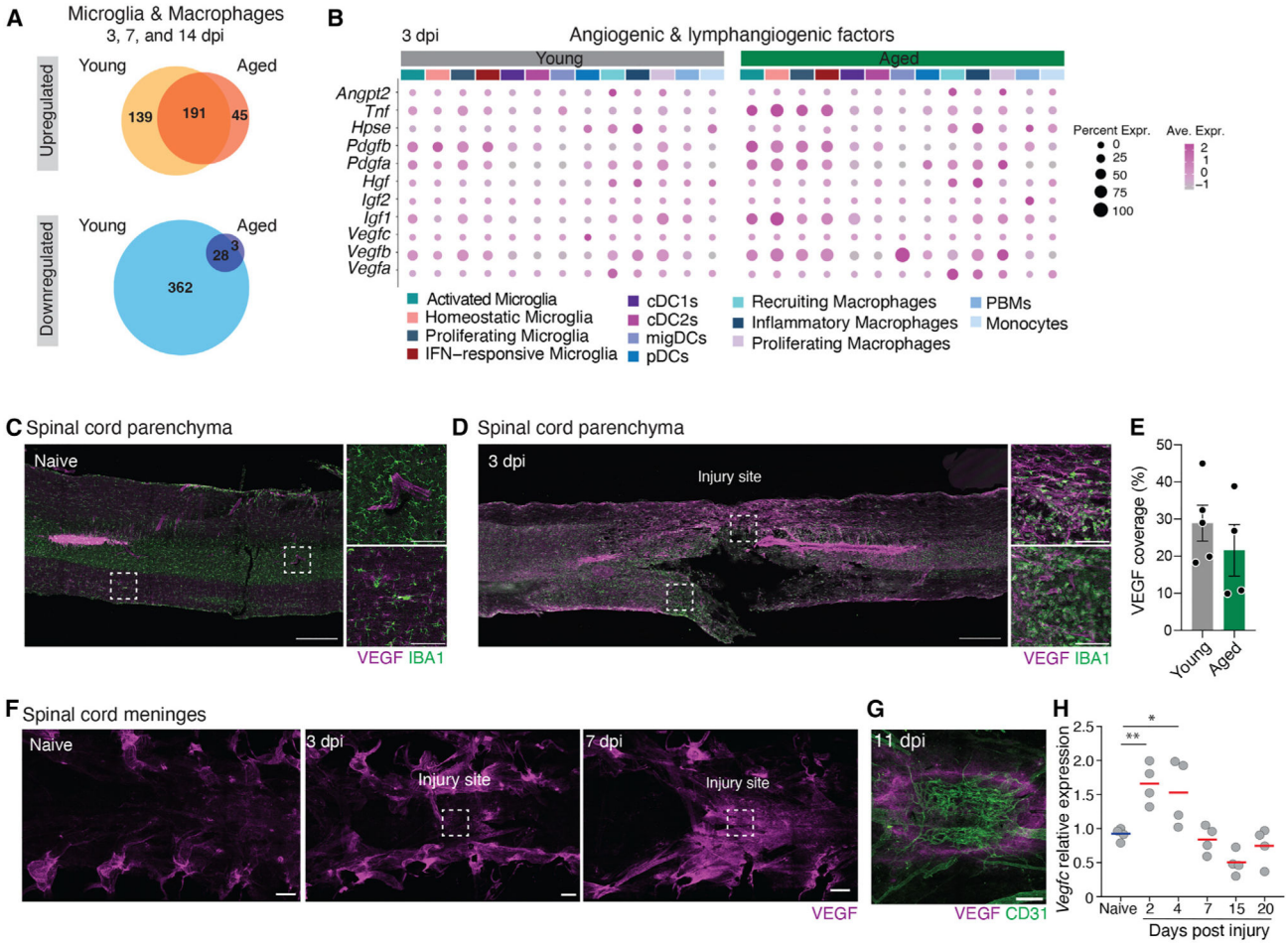

Figure 3. Contusion injury induces expression of angiogenic factors in the spinal cord and the meninges

(A) Pie charts illustrating the overlap between the upregulated and downregulated DEGs in microglial and macrophage clusters combined (shown in Figures 1A-1D) of young and aged mice across all injury time points.

(B) Heatmap showing the scaled expression of selected angiogenic genes and lymphangiogenic genes for all myeloid cell populations identified in Figures 1F and 2A.

(C) Immunohistochemistry of VEGF expression in the naive spinal cord of young mice. Scale bars, 500 and 100 μm. Representative image of n = 2 mice.

(D) Immunohistochemistry of VEGF expression in spinal cord sections and its co-localization in IBA1^{+} cells after injury (3 dpi) of young mice. Scale bars, 500 and 100 μm. Representative image of n = 3 mice.

(E) Quantification of VEGF coverage in the spinal cord 3 dpi by immunohistochemistry. n = 5 young and 4 aged mice. Data are presented as mean ± SEM. Significance was determined using two-tailed Mann-Whitney test.

(F) Immunohistochemistry of VEGF expression in the spinal cord meninges of naive and injured (3 and 7 dpi) young mice. Scale bars, 500 μm. Representative image of n = 2 mice.

(G) Immunohistochemistry of VEGF expression and CD31^{+} blood vessels in the spinal cord meninges at the contusion site. Scale bars, 200 μm. Representative image of n = 3 mice.

(H) Quantitative real-time PCR analysis of Vegfc in homogenates of the spinal cord meninges from young mice after contusion injury. n = 4 mice per group. Significance was determined using one-way ANOVA with Tukey's post hoc test. *$p < 0.05$ and **$p < 0.01$. See also Table S5.

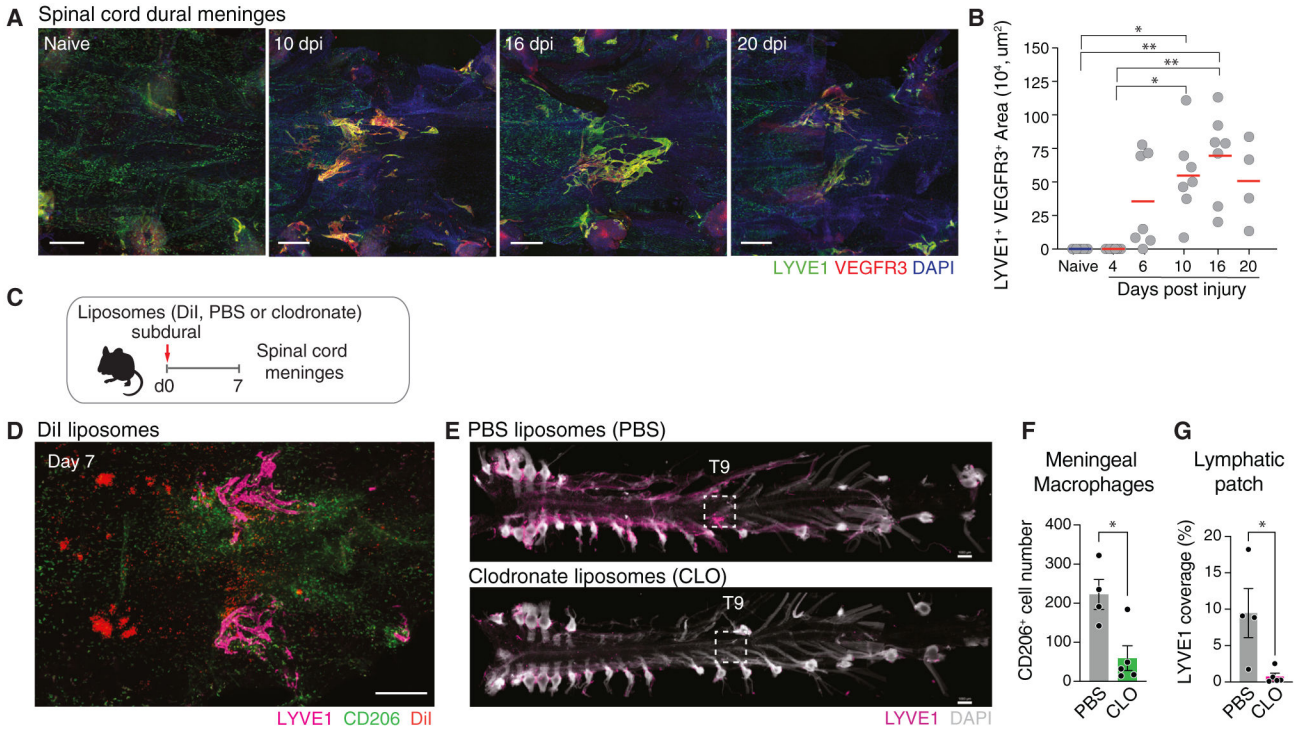

Figure 4. Meningeal macrophages support lymphangiogenesis of spinal cord meningeal lymphatic vessels after injury

(A and B) (A) Immunohistochemistry and (B) quantification of the spinal cord meninges at the contusion site, highlighting the formation of LYVE1$^+$ VEGFR3$^+$ lymphatic vasculature after spinal cord injury of young mice. Scale bars, 1,000 μm. Each dot represents an individual mouse. n = 4–7 mice per time point. Data are presented as mean ± SEM. Significance was determined using one-way ANOVA with Tukey's post hoc test. *p < 0.05 and **p < 0.01.

(C) Mice were given a laminectomy and subdural injection at thoracic vertebra 9 (T9) of liposomes containing either fluorescent DiI, PBS, or clodronate.

(D) Immunohistochemistry of LYVE1$^+$ vessels, CD206$^+$ macrophages, and DiI liposomes in the spinal cord meninges 7 days after laminectomy and subdural injection. Scale bars, 1,000 μm. Representative of n = 5 adult mice.

(E) Immunohistochemistry of LYVE1$^+$ lymphatic vessels 7 days after laminectomy and subdural PBS or clodronate liposome injection. Dotted lines indicate the injection site. Scale bars, 1,000 μm.

(F and G) (F) Quantification of CD206$^+$ macrophage numbers and (G) LYVE1$^+$ coverage in the spinal cord meninges 7 days after injection. n = 4 young and 5 aged mice. Data are presented as mean ± SEM. Significance was determined using two-tailed Mann-Whitney test, *p < 0.05.

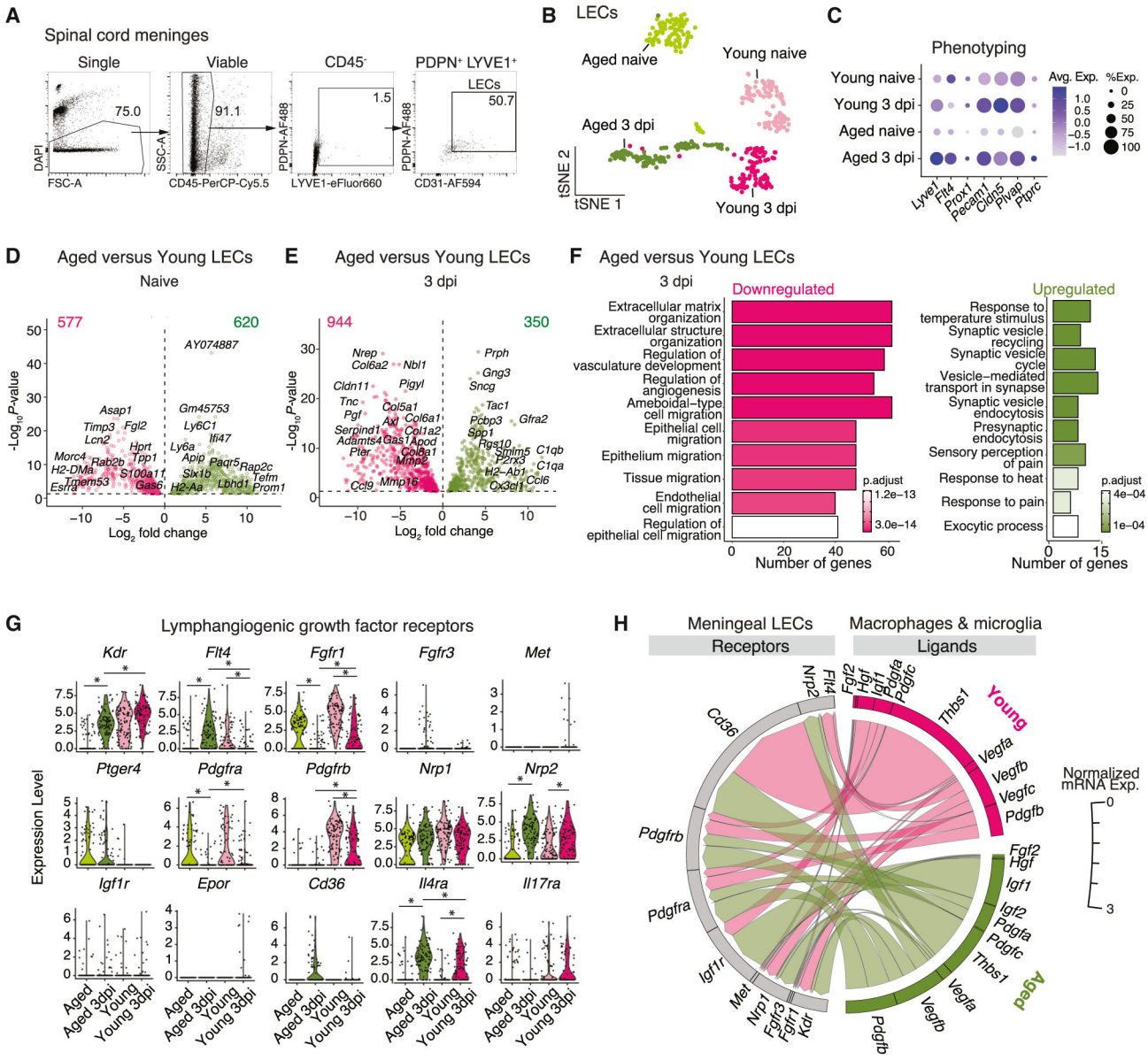

Figure 5. Transcriptomic analysis reveals signaling axis between myeloid cells in the spinal cord and meningeal lymphatic endothelial cells

(A) Flow cytometry gating strategy for the isolation of lymphatic endothelial cells (LECs) from the spinal cord meninges.

(B) tSNE visualization of scRNA-seq analysis of LECs isolated from the meninges of young and aged mice, naive or 3 dpi. n = 5 pooled for naive young, 3 dpi young, and naive aged; n = 3 pooled for 3 dpi aged.

(C) Dot plot demonstrating expression of LEC phenotyping markers.

(D and E) Volcano plot showing differentially expressed genes (DEGs) between (D) aged and young naive and (E) injured (3 dpi) LECs.

(F) GO terms associated with downregulated and upregulated DEGs between aged and young LECs shown in (E).

(G) Violin plots demonstrating lymphangiogenic growth factor receptor expression in meningeal LECs from young and aged mice. *p.adjust < 0.05. Significance was determined using an F test applied to the generalized linear regression model with adjusted denominator degrees of freedom.

(H) Predicted receptor-ligand interactions between lymphangiogenic factors in macrophages and microglia from the spinal cord of 3 dpi mice and ligands in spinal cord meningeal LECs. The ligands in pink are derived from young and those in green are from aged mice (Figure 3B). The receptors denoted in gray were derived from the analysis of spinal cord meningeal LECs shown in Figure 5G.

See also Figure S5 and Table S6.

KEY RESOURCES TABLE

REAGENT or RESOURCE	SOURCE	IDENTIFIER
Antibodies		
Anti-CD11b BUV563 (Clone M1/70)	BD Biosciences	Cat# 741242; RRID: AB_2870793
Anti-CD11c BUV737 (Clone N418)	BD Biosciences	Cat# 749039; RRID: AB_2873433
Anti-CD19 BV480 (Clone 1D3)	BD Biosciences	Cat# 566107; RRID: AB_22739509
Anti-CD206 AF488 (Clone C068C2)	Biolegend®	Cat# 141709; RRID: AB_10933252
Anti-CD31 AF594 (Clone 390)	Biolegend®	Cat# 102432; RRID: AB_2617017
Anti-CD4 BUV395 (Clone GK1.5)	BD Biosciences	Cat# 740208; RRID: AB_2734761
Anti-CD45 BV750 (Clone 30-F11)	BD Biosciences	Cat# 746947; RRID: AB_2871734
Anti-CD45 PerCP-Cy5.5 (Clone 30-F11)	Biolegend®	Cat# 103132; RRID: AB_893340
Anti-CD64 PE (Clone X54-5/7.1)	Biolegend®	Cat# 139304; RRID: AB_10612740
Anti-CD64 PerCP-Cy5.5 (Clone X54-5/7.1)	Biolegend®	Cat# 139308; RRID: AB_2561963
Anti-CD8a AF532 (Clone 53-6.7)	eBioscience™	Cat# 58-0081-80; RRID: AB_11218685
Anti-CX3CR1 BV650 (Clone SA011F11)	Biolegend®	Cat# 149033; RRID: AB_2565999
Anti-E-cadherin AF647 (Clone DECMA-1)	Biolegend®	Cat# 147307; RRID: AB_2563954
Anti-F4/80 AF700 (clone BM8)	Biolegend®	Cat# 123130; RRID: AB_2293450
Anti-Ki67 AF488 (Clone 16A8)	Biolegend®	Cat# 652410; RRID: AB_2562141
Anti-Ki67 BV421 (Clone 16A8)	Biolegend®	Cat# 652411; RRID: AB_2562663
Anti-Ki67 PE (Clone 16A8)	Biolegend®	Cat# 652403; RRID: AB_2561524
Anti-Ly6C AF488 (Clone HK1.4)	Biolegend®	Cat# 128022; RRID: AB_1060820
Anti-Ly6C PerCP-Cy5.5 (Clone HK1.4)	Biolegend®	Cat# 128012; RRID: AB_1659241
Anti-Ly6G BUV661 (Clone 1A8)	BD Biosciences	Cat# 741587; RRID: AB_2871000
Anti-Lyve1 eFluor660 (Clone ALY7)	eBioscience™	Cat# 50-0443-82; RRID: AB_10597449
Anti-MHCII I-A/I-E BV510 (Clone M5/114.15.2)	Biolegend®	Cat# 107635; RRID: AB_2734168
Anti-MHCII I-A/I-E PE-Cy7 (Clone M5/114.15.2)	eBioscience™	Cat# 25-5321-82; RRID: AB_10870792
Anti-P2RY12 APC (Clone S16007D)	Biolegend®	Cat# 848006; RRID: AB_2721469
Anti-Podoplanin AF488 (Clone 8.1.1)	Thermo Fisher	Cat# 53-5381-82; RRID: AB_1106990
Anti-TCRb BUV805 (Clone H57-597)	BD Biosciences	Cat# 748405; RRID: AB_2872824
Anti-XCR1 BV421 (Clone ZET)	Biolegend®	Cat# 148216; RRID: AB_2565230
Anti-CD206 (Clone MR5D3)	Bio-Rad	Cat# MCA2235; RRID: AB_324622
Anti-CD31 (Clone 2H8)	Millipore	Cat# MAB1398Z; RRID: AB_94207
Anti-CD68 (Clone FA-11)	Abcam	Cat# ab53444; RRID: AB_869007
Anti-Collagen 1	Abcam	Cat# ab270993; RRID: AB_2927551
Anti-GFAP	Millipore	Cat# AB5541; RRID: AB_177521
Anti-Iba1	Abcam	Cat# ab5076; RRID: AB_2224402
Anti-Ki67	Abcam	Cat# ab15580; RRID: AB_443209
Anti-Laminin (1+2)	Abcam	Cat# ab7463; RRID: AB_305933
Anti-TMEM119 (Clone E3E10)	Cell Signaling Technology	Cat# 90840; RRID: AB_2928137
Anti-VEGF (Clone SP07-01)	Thermo Fisher	Cat# MA5-32038; RRID: AB_2809332
Anti-VEGFR3	R&D Systems	Cat# AF743; RRID: AB_355563

REAGENT or RESOURCE	SOURCE	IDENTIFIER
Anti-Armenian hamster AF488	Jackson Immunoresearch	Cat# 127-545-160; RRID: AB_2338997
Anti-Goat IgG AF594	Thermo Fisher	Cat# A32758; RRID: AB_2762828
Anti-Rabbit IgG AF647	Thermo Fisher	Cat# A32795; RRID: AB_2762835
Anti-Rat IgG AF488	Thermo Fisher	Cat# A21470; RRID: AB_10561519
Chemicals, peptides, and recombinant proteins		
ACK Lysis Buffer	Quality Biological	Cat# 118-156-101CS
Brilliant Stain buffer Plus	BD Biosciences	Cat# 566385
Chicken serum, USA origin	Sigma	Cat# C5405
Clodronate Liposomes (Clodrosome®)	Encapsula Nano Sciences	Cat# CLD8901
Collagenase VIII	Sigma	Cat# C2139
Control Liposomes (Encapsome®)	Encapsula Nano Sciences	Cat# CLD8901
DAPI	Sigma	Cat# D9542
DNAse I	Sigma	Cat# DN25
Fetal bovine serum	Thermo Fisher	Cat# 15000044
Fluoroliposome®-Dil	Encapsula Nano Sciences	Cat# CLD8911
FluorSave™	Millipore	Cat# 345789
Formic acid	Thermo Scientific	Cat# 270480250
Foxp3/Transcription Factor staining kit	eBioscience	Cat# 00-5523-00
Goat serum	Vector Laboratories	Cat# S-1000-20
Heparin Sodium	Fisher Scientific	Cat# H19
Low endotoxin heat shock BSA powder	Fisher Scientific	Cat# 50-253-924
LS columns	Mitenyi Biotec	Cat# 130-042-401
Neutral buffered formalin (10%)	Fisher Scientific	Cat# SF100-4
Opal 570 Reagent Pack	Perkin Elmer	Cat# FP1488001KT
Opal 690 Reagent Pack	Perkin Elmer	Cat# FP1497001KT
Paraformaldehyde, Aqueous EM grade (16%)	Fisher Scientific	Cat# 50-980-487
ProLong Gold	Thermo Fisher	Cat# P36934
Purified anti-mouse CD16/32 (Fc block)	Biolegend®	Cat# 101302
Recombinant RNase inhibitor	Takara Bio	Cat# 2313A
RNAscope Target Probe Irf7-C1	Advanced Cell Diagnostics	Cat# 534541
RNAscope Target Probe Sall1-C3	Advanced Cell Diagnostics	Cat# 469661-C3
Single cell 10x Lysis buffer	Takara Bio	Cat# 635013
Sodium citrate dihydrate	Sigma	Cat# W302600
Tissue-Plus O.C.T. compound, clear	Thermo Fisher	Cat# 23-730-571
Trypan blue	Thermo Fisher	Cat# 15250061
TRIzol reagent	Thermo Fisher	Cat# 15596026
UltraPure™ non-acetylated BSA	Thermo Fisher	Cat# AM2616
Viastain™ AOPI staining solution	Fisher Scientific	Cat# CS2-0106
Zombie NIR fixable viability kit	Biolegend®	Cat# 423102
Critical commercial assays		
CD45 Microbeads, UltraPure, mouse	Miltenyi Biotec	Cat# 130-052-301

REAGENT or RESOURCE	SOURCE	IDENTIFIER
Chromium Single cell 3' Library & Gel Bead Kit	10X Genomics	Cat# PN-120267
High-capacity cDNA reverse transcription kit	Applied Biosystems	Cat# 4368814
RNAscope Multiplex Fluorescent Reagent Kit v2	Advanced Cell Diagnostics	Cat# 323100
Deposited data		
Fastq files and quantified gene counts for single-cell sequencing	Gene Expression Omnibus (GEO)	GEO: GSE205038
Experimental models: Organisms/strains		
C57BL/6	The Jackson Laboratory	JAX000664
B6(Cg)-B6(Cg)-*Ifnar1*$^{tm1.2Ees}$/J	The Jackson Laboratory	JAX028288
B6.129-*Ifnb1*^{tm1Lky}/J	The Jackson Laboratory	JAX010818
B6.129S4-*Ifng*$^{tm3.1Lky}$/J	The Jackson Laboratory	JAX017581
Software and algorithms		
ImageJ	Schneider et al.[93]	https://imagej.nih.gov/ij/; RRID: SCR_003070
FIJI package for ImageJ	Schneider et al.[93]	https://imagej.net/Fiji; RRID: SCR_002285
FlowJo v10.8	BD	https://www.flowjo.com/; RRID: SCR_008520
Prism v9.3.0	GraphPad, Dotmatics	https://www.graphpad.com/scientific-software/prism/; RRID: SCR_002798
R studio	R studio	https://rstudio.com/
Illumina Bcl2 fastq software	Illumina	https://support.illumina.com/downloads/bcl2fastq-conversion-software-v2-20.html
Seurat pipeline for R studio	Butler et al.[94]	https://satijalab.org/seurat/articles/install.html; RRID: SCR_016341
Cellranger software pipeline	10X Genomics	https://support.10xgenomics.com/single-cell-gene-expression/software/pipelines/latest/installation; RRID: SCR_023221
Primer-Blast	NCBI-NIH	https://www.ncbi.nlm.nih.gov/tools/primer-blast/; RRID: SCR_003095
Custom code for RNA sequencing data analysis	This paper	https://zenodo.org/record/7604317
Other		
Mini Bead beater	Biospec Products	Cat# C321001
Impact Horizon Impactor	Precision Systems and Instrumentation	Cat# IH-0400